Effective Charges Near 56Ni and Production of Anti-Nuclei Studied with Heavy-Ion Reactions

du Rietz, Rickard

2005

Effective Charges Near ^{56}Ni and Production of Anti-Nuclei Studied with Heavy-Ion Reactions

Rickard du Rietz
Department of Physics

LUND UNIVERSITY

2005

Thesis for the Degree of Doctor of Philosophy

To be presented, with the permission of the Faculty of Natural Science of Lund University, for public criticism in lecture hall B at the Department of Physics on March 3^{rd} 2005, at 10.15.

Faculty opponent: Dr. Cyrus Baktash
Oak Ridge National Laboratory, USA

Division of Nuclear Physics
Department of Physics
Lund University
Box 118
SE-221 00 Lund
Sweden

ISRN LUNFD6/(NFFR-1026)/1-152/ (2005)
ISBN 91-628-6394-0

Typeset by the author using LaTeX 3.14159
Printed in Sweden by Intellecta DocuSys AB, Malmö 2005

Organization **LUND UNIVERSITY** Department of Physics Lund University Box 118 SE-221 00 Lund SWEDEN	**Document name** **DOCTORAL DISSERTATION** **Date of issue** January 20, 2005 **CODEN** ISRN LUNFD6/(NFFR-1026)/1-152/(2005)
Author(s) Rickard du Rietz	**Sponsoring organization**

Title and subtitle
Effective Charges Near ^{56}Ni and Production of Anti-Nuclei Studied with Heavy-Ion Reactions

Abstract
This thesis presents the research performed within two different research groups using heavy-ion induced nuclear reactions. They offer the opportunity to investigate different properties of nuclear matter. The results are based on measurements using a variety of different experimental techniques.

The PHENIX experiment measured the production of deuteron and anti-deuterons at mid-rapidity in gold-gold collisions at the Relativistic Heavy-Ion Collider, RHIC. The invariant yields and transverse momentum spectra are presented. The results are not in agreement with a simple coalescence model with a constant coalescence parameter B_2.

Excited states of atomic nuclei were populated using fusion-evaporation reactions. The emitted γ rays were detected in large multi-detector arrays. One experiment was in conjunction with a plunger device. Lifetimes of analogue states in the $T_z = \pm 1/2$ $A = 51$ mirror nuclei ^{51}Fe and ^{51}Mn were measured using the recoil distance Doppler shift (RDDS) technique. The deduced $B(E2)$ values make possible an investigation of isoscalar and isovector polarization charges. A comparison between the experimental results and large-scale shell-model calculations yields a quantitative estimate of the effective nucleon charges in the fp shell.

Key words:
Heavy-ion reactions, PHENIX, RHIC, anti-deuteron, γ ray multi-detector arrays, fusion-evaporation reactions, RDDS, mirror nuclei, lifetimes, effective charges, shell-model calculations

Classification system and/or index terms (if any)

Supplementary bibliographical information:		**Language** English
ISSN and key title:		**ISBN** 91-628-6394-0
Recipient's notes	**Number of page** 152	**Price**
	Security classification	

Preface

This thesis is the result of my years as a graduate student at the Physics Department at Lund University. It compiles the work I have been involved in, which has been performed within two different research groups. Both groups perform experiments with heavy-ion induced nuclear reactions to investigate the properties of nuclear matter.

During my first years as a student I was involved in the research activities of the group for Relativistic Heavy-Ion Physics. This research group is participating in the PHENIX experiment, which is one of four experiments at the Relativistic Heavy-Ion Collider at Brookhaven National Laboratory, USA. In particular, the group is contributing to the pad chamber detectors. I have also been involved in the work with the Lund PC Farm, which has been used for various simulations to the PHENIX experiment. The analysis of data has focused on the search for deuterons and anti-deuterons produced in the heavy-ion collisions. Most of my work within this research group is discussed in my licentiate thesis, which was defended during spring 2003.

During my further studies I have been involved in the research activities of the Nuclear Structure Group, which aim to investigate properties and structures of atomic nuclei. I have participated in several experiments and is the spokesperson for an upcoming experiment in preparation. The analysis work has focused on lifetime measurements in data from the GASP03.12 experiment performed at Legnaro National Laboratory, Italy, during 2003. Based on the experimental results I have performed an unique study to probe effective nucleon charges in the fp shell.

I have previously presented parts of the results at the following occasions:

- Quark Matter Conference, Nantes, France, July, 2002.
- 12^{th} UK Postgraduate Nuclear Physics Summer School, St. Andrews, Scotland, September, 2003.
- Svenskt Kärnfysikermöte XXIII, Stockholm, Sweden, November, 2003.
- 4^{th} International Balkan School on Nuclear Physics, Bodrum, Turkey, September 2004.

The first chapter of the thesis gives a short introduction to the nuclear shell-model and the quark-gluon plasma. It also briefly describes nuclear reactions and the reaction mechanisms that have been employed in this work.

The next chapter presents the experiments this thesis is based upon. In particular the GASP03.12 and PHENIX experiments are described. Chapter two also introduce the utilized methods for the lifetime analyses.

The analysis of deuterons and anti-deuterons is described in detail in chapter three. This analysis is one of two independent searches for deuterons and anti-deuterons performed with PHENIX.

Chapter four introduces and describes electromagnetic properties in nuclei. In particular, the phenomenon of effective charges is discussed. The chapter further describes the various analyses I have been involved in.

Lund, January 20, 2005
Rickard du Rietz

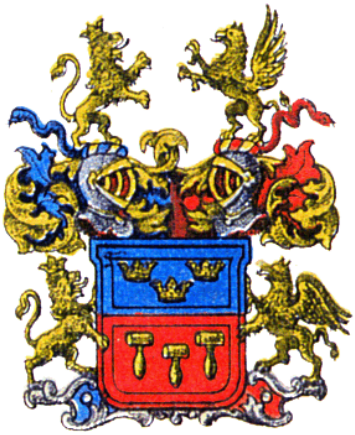

The du Rietz coat of arms with attributes.

List of Included Papers

PAPER I: **Construction and Performance of the PHENIX Pad Chambers**
K. Adcox *et al.* (PHENIX collaboration)
Nucl. Instr. and Meth. A **497** *(2003) 263*

PAPER II: **Deuteron and antideuteron production in Au+Au collisions at $\sqrt{S_{NN}} = 200$ GeV**
S.S. Adler *et al.* (PHENIX collaboration)
Submitted to Phys. Rev. Lett.

PAPER III: **Effective Charges in the *fp* Shell**
R. du Rietz *et al.*
Phys. Rev. Lett. **93** *222501 (2004)*

PAPER IV: **Lifetime Measurements in the $A = 51$ Mirror Nuclei**
R. du Rietz, J. Ekman, C. Fahlander, and D. Rudolph
Proceedings of the 4^{th} International Balkan School on Nuclear Physics, Bodrum, Turkey, September 2004. To be published in Balkan Physics Letters Special Issue

PAPER V: **A Shell-Model Study of ^{53}Fe**
R. du Rietz *et al.*
To be submitted to Phys. Rev. C

Contents

Chapter 1

General Aspects

During the first moment of its evolution, the universe was formed through several phase transitions involving fundamental changes in the state of matter. After the first few microseconds, matter is believed to have existed in a state described as a soup of free quarks and gluons, the Quark Gluon Plasma. As the universe expanded and cooled down, more complex matter condensed out of the plasma, eventually forming atomic nuclei and finally the atoms, which are the basis for any known life form today. At present, it is believed that a Quark Gluon Plasma may exist in the universe in the core of neutron stars. While the temperature is relatively low in the stars, the density is extremely high due to immense gravitational forces. In todays laboratory nucleus-nucleus collisions are used to ignite nuclear matter that form highly excited systems. With advanced and complex detector equipment the constituents and evolution of such reactions are investigated, which allows to probe fundamental properties and changes of nuclear matter in the course of the evolution of the universe.

1.1 Nuclear Matter

Nuclear matter has been studied ever since Rutherford's famous scattering experiment revealed that the atom consists of a small, positively charged nucleus, surrounded by electrons. A few years after this discovery it was realized that the nucleus itself consisted of nucleons (protons and neutrons) and later experiments revealed that even the nucleons had an internal structure, namely the quarks. The quarks are combined in groups of two or three forming the hadrons, which consists of mesons (two quarks) and baryons (three quarks). The transition from ordinary nuclear matter to quark matter (or vice-versa) is predicted to behave like a thermodynamical phase transition, analogous to the transition from water to steam during boiling. A schematic phase diagram for nuclear matter is sketched in Fig. 1.1 that shows temperature vs net baryon density for an extended volume of nuclear matter in thermal equilibrium. The indicated trajectory illustrates an avenue for probing quark matter using high-energy nucleus-nucleus collisions, where conditions may approximate those of the early universe.

Nucleus-nucleus collisions are also employed to investigate properties of nuclear matter near its ground state (as indicated in Fig. 1.1). Such studies allows to probe

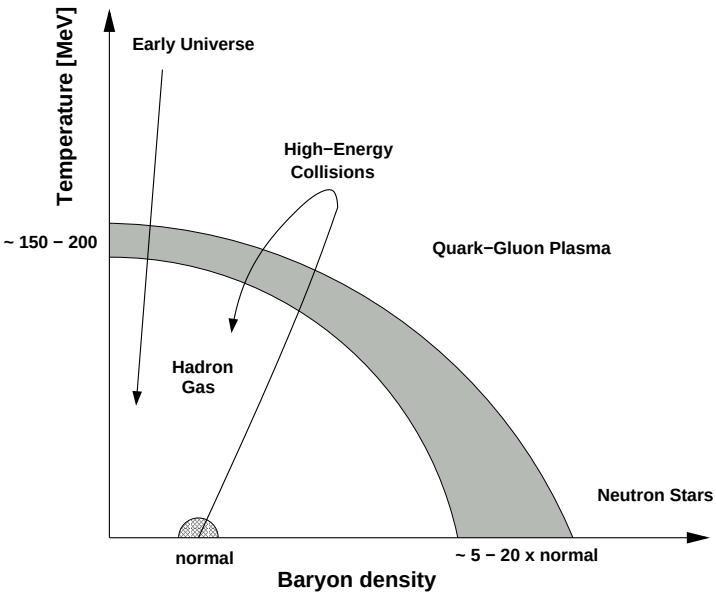

Figure 1.1: *Phase diagram of nuclear matter. Temperature is plotted vs net baryon density for an extended volume of nuclear matter in thermal equilibrium.*

parameters used to describe a nucleus: its mass, nuclear radius, angular momentum, electromagnetic moments, energies of excited states, etc. This in turn offers a possibility to investigate the properties of the force acting between the nucleons. However, to obtain an understanding and deeper knowledge of nuclear properties it is, like in any other regime in Fig 1.1, important to perform comparisons of experimental data to theoretical calculations and simulations. Thus it is required to formulate a theoretical model that accounts for the nuclear force between nucleons, which can be used to describe a nuclear system. One such nuclear model is the *nuclear shell model* [1, 2], which successfully describes near-spherical nuclei and serves as a base for other, more complex models.

1.1.1 The Nuclear Shell Model

In the nuclear shell model, the nucleons (protons and neutrons) are assumed to move in bound orbitals. Each orbital is assigned a set of quantum numbers and has a well determined energy, angular momentum, and parity associated with it. As the nucleons are fermions (half-integer spin) the Pauli principle permits no more than two nucleons (of each type) to occupy the same state, i.e. have identical sets of quantum numbers. This results in a finite number of particles occupying a given energy level and a nucleus is predicted to have a shell structure. When a shell with particular energy, angular momentum, and parity is filled, any additional particle of that type

must be put into a different shell at a higher energy. The concept of closed (filled) shells is supported from experimental data, which indicates that closed shells occur at proton or neutron numbers of 2, 8, 20, 28, 50, 82, and 126, the so-called magic numbers.

A nucleus consist of a given number of individual nucleons. The properties of the nuclear system can be described from the solutions to the Schrödinger wave equation. Due to mathematical difficulties solving this full many-body problem the Schrödinger wave equation cannot be solved analytically for a given Hamiltonian, but must be solved using numerical methods. Assuming only a two-body nucleon interaction[1], the Hamiltonian for such an A-nucleon system can be written as

$$\mathcal{H} = \sum_{i=1}^{A} \left(-\frac{\hbar^2}{2m} \nabla_i^2 \right) + \frac{1}{2} \sum_{i \neq j}^{A} V_{ij}(\vec{r}), \tag{1.1}$$

where the first term is the kinetic energy of the particle motion and $V_{ij}(\vec{r})$ is the two-body potential representing the interaction between the nucleons i and j. As the nuclear force affecting the nucleons is not fully understood, the nucleon-nucleon interaction is commonly approximated with an average nuclear potential. This potential should represent the average interaction of all the other nucleons exerted on any one of the nucleons in the nucleus. Usually, a spherically symmetric potential is selected, which allows to separate the Schrödinger equation into a radial part and an angular part, where the latter is independent of the central potential $V(r)$. Hence, the angular part can be solved directly and the solution can be expressed as the *spherical harmonics*, $Y_{\ell m_\ell}(\theta, \phi)$. The introduced quantum number $\ell = 0, 1, 2, ...$ in $Y_{\ell m_\ell}(\theta, \phi)$ is related to the orbital angular momentum and its projection onto the quantization axis is given by $m_\ell = 0, \pm 1, \pm 2, ..., \pm \ell$. Each ℓ-value can be represented as a nuclear orbital (level) denoted as $s, p, d, f, g, ...$ Due to the restriction on m_ℓ there are exactly $2l + 1$ possible $Y_{\ell m_\ell}(\theta, \phi)$ solutions for each level. Thus a $2l + 1$ folded degeneracy is introduced, which together with the intrinsic spin, allows for an occupancy of $2(2l+1)$ nucleons in one orbital. In combination with the solution to the radial part, using the potential representing the nucleon-nucleon interaction, the levels are separated in energy and a shell structure is obtained. The choice of the shell model potential should thus be of such form that experimentally observed shell structures are reproduced.

One first attempt to introduce a potential representing the average interaction is the spherical harmonic oscillator potential. Comparison with experimental data reveals, however, that only the magic numbers of 2, 8, and 20 are reproduced in the obtained shell structure. To obtain a better agreement with observed data a more realistic potential describing the average interaction with the other nucleons is introduced. Such a potential mimics the nuclear matter or charge distribution and is expressed using a spherical Woods-Saxon form written as

$$V_{WS}(r) = \frac{-V_0}{1 + exp(\frac{r-R}{a})}, \tag{1.2}$$

which is sketched in Fig. 1.2. r is the distance of the nucleons with respect to the center of the nucleus and R is the radius of the nucleus given by $R = r_o A^{1/3}$ fm

[1] In reality, however, there is evidence to suggest that the nucleons interact not only through two-body forces, but through three-body forces as well.

($r_0 \approx 1.2$ fm). The depth of the well, V_0, is proportional to the density of nucleons and is of the order of 50 MeV. The parameter $a \approx 0.57$ fm is related to the surface diffuseness, d, which is the distance over which the potential changes from 90% to 10% of V_0 (see Fig. 1.2).

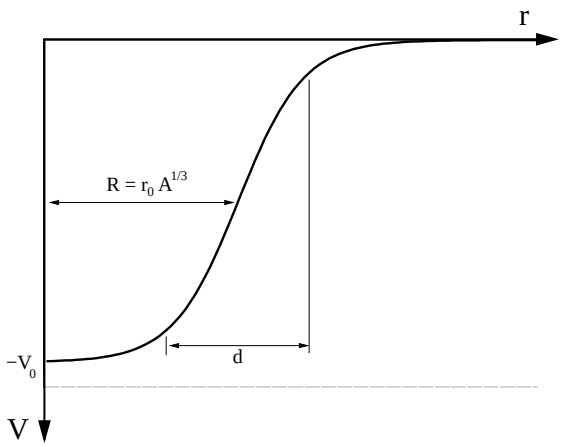

Figure 1.2: *The form of a Woods-Saxon potential often used in shell model calculations. The skin diffuseness, d, is defined as the distance from 90% to 10% of the total potential depth.*

The level structure predicted by the shell model using the Woods-Saxon potential is illustrated in Fig. 1.3(a). It is found that neither the spherical harmonic oscillator potential, nor the Woods-Saxon potential produces energy eigenvalues with closed shells for all the magic numbers. This is, however, accounted for by adding yet another term to Eq. 1.2, which allows for even further separation of the energy levels. The introduced term, referred to as the *spin-orbit* interaction, couples the orbital angular momentum with the intrinsic spin to form a total angular momentum $\vec{j}$ with an associated quantum number j. Due to the two orientations of the nucleon spin the spin-orbit interaction splits the degeneracy of an energy level at a given ℓ-value ($\ell > 0$) into two new levels with different energies and total angular momentum quantum number $j = \ell \pm 1/2$. Furthermore, the ℓ-value determines the parity of the level such that an even (odd) ℓ-value corresponds to positive (negative) parity. Figure 1.3(b) shows the energy level structure calculated using the spin-orbit interaction added to the Woods-Saxon potential. The energy levels are denoted with quantum numbers $n\ell j$ and as seen the experimental observed magic numbers are well reproduced.

The described nuclear shell model is employed as a first attempt to predict the properties of nuclei in or near their ground states. Regardless of its simplicity it is found to predict many nuclear properties very well. However, in the above approach it is assumed that the nucleus can be viewed as a spherical system, which is not the case for all nuclear systems. Some nuclei are deformed in their ground states and nuclei that are spherical, in their ground state, may reveal a deformation in an excited state. Hence, for such a scenario the spherical shell model fails to predict the nuclear properties and thus other models are introduced to account for these phenomena.

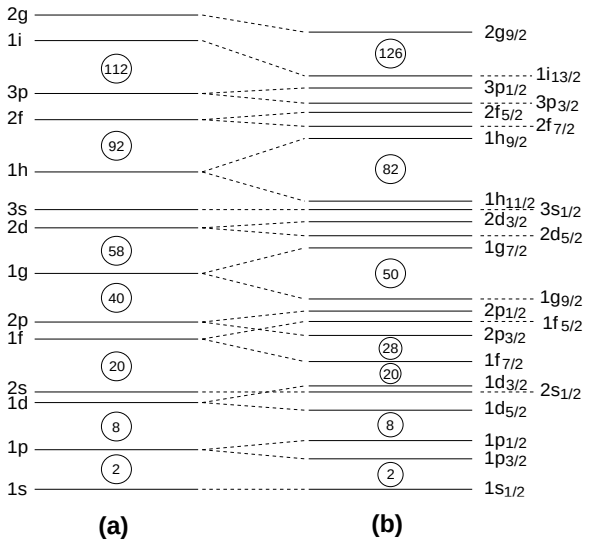

Figure 1.3: *The energy levels predicted by the shell model using a Woods-Saxon form on the nuclear potential. Panel (a) shows the obtained level structure without any spin-orbit interaction added to the potential whereas panel (b) shows the results including ℓs coupling. The observed magic numbers are nicely reproduced for the latter case.*

Such models are, e.g., the Nilsson model, in which deformation is introduced, and the Cranking model that treats rotating deformed nuclei.

Relevant parts of the present thesis discuss nuclear properties using a perspective based on large-scale shell-model calculations. In particular nuclei distributing their valence nucleons, i.e. nucleons outside a closed shell, in the fp shell have been investigated. The calculations employed an inert ^{40}Ca core, representing the $N = Z = 20$ shell closure, and the valence nucleons distributed in the full fp shell, which contains the $1f_{7/2}$ orbit below and the $2p_{3/2}$, $1f_{5/2}$, and $2p_{1/2}$ orbits above the $N = Z = 28$ shell closure.A more detailed description of the shell-model calculations is found in Ref. [3].

1.1.2 The Quark Gluon Plasma

The properties and structures of nuclei are predicted using theoretical models (e.g. the nuclear shell model), where nucleons are used as building blocks to describe the nuclei. However, the nucleons have an internal structure, quarks, which are supposed to be the fundamental constituents of nuclear matter. The quarks are affected by the strong force, which in the standard model is described by Quantum Chromo Dynamics, QCD.

The quarks are fermions and in this model they are assigned an electrical as well as a color charge. In nature only color neutral objects are allowed, which indicates that there can exist no free quarks. Instead they combine together in the form of hadrons.

The hadrons are combinations of either three quarks or anti-quarks (qqq or $\bar{q}\bar{q}\bar{q}$), as in baryons[2], or of one quark and one anti-quark ($q\bar{q}$), as in mesons[3]. Without the color charge a hadron like Δ^{++}, which consists of three upquarks (u), should have been forbidden as the quarks have to obey the Pauli exclusion principle. However, such a combination of three u quarks may be formed using three different color charges, which creates a color neutral object. The color charge is denoted red, blue, and green with the corresponding anti-colors.

The gluons, which carry color but no electric charge, are the exchange particles of the strong force. As they carry color they couple not only to the quarks, but also to each other. As a result the effective color charge will be screened at short distances. In QCD, the strength of the strong force affecting the quarks and gluons becomes relatively weak for short distances but increases rapidly for larger separations (> 1 fm). Hence, for nuclear matter close to its ground state, quarks and gluons are confined to the hadrons, whereas at large baryon densities and high temperatures the theory predicts that they are no longer confined [4, 5]. Instead they may be free to move within the whole system, forming a state of matter referred to as the Quark-Gluon Plasma, QGP. Today relativistic nucleus-nucleus collisions are used to create conditions with extreme temperatures and densities where normal nuclear matter may undergo a phase transition towards a QGP (see Fig. 1.1). The space-time evolution of such a phase transition created in a relativistic heavy-ion collision is sketched in Fig. 1.4 [4]. In this picture the collision between the nuclei occur at $(z, t) = (0, 0)$, where z is the position coordinate along the beam axis and t the time coordinate. The remnants

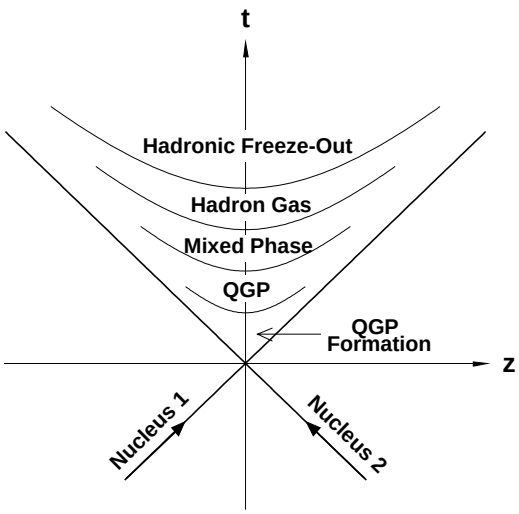

Figure 1.4: *Space-time evolution of a nucleus-nucleus collision where a QGP is formed.*

[2]The proton and the neutron are examples of baryons.
[3]For example the *pi* mesons or the K mesons.

of the incoming nuclei fly away from the central region leaving behind a system of strongly interacting matter, which expands both longitudinally and transversely. If a phase transition to a QGP occurs the quarks and gluons become deconfined. The system will remain in this state until the expansion has reduced the temperature and baryon density enough to form hadrons and to become stable. Directly after this mixed phase the system exists in the form of a hadron gas, where the density and temperature is still too high for the hadrons to escape without further interactions. Eventually, at some point during the expansion, the interactions between the hadrons will cease and the system reaches thermal freeze-out.

The hadrons emitted from the collision reflect the properties of the system at the final freeze-out. Interesting parameters such as temperature, source size, etc. can be determined from the hadronic spectra. The time of freeze-out may differ for different particle species, and thus give rise to different source radii and temperatures. The temperature of a system is a measure of the kinetic energy of its constituent. As a large fraction of the longitudinal momentum stems from the longitudinal expansion, and therefore is of non-thermal origin, one usually determines the temperature from the transverse momentum of the emitted particles, p_T. A rough estimate is $T \sim \langle p_T \rangle$. The dimensions of the particle emitting source can be determined by intensity interferometry. This method, often referred to as Hanbury-Brown-Twiss (HBT) correlations, measures the correlation between two identical particles (e.g. $\pi^+\pi^+$) emitted from the source [6]. From this information it is in principle possible to determine both the longitudinal and transverse size of the source. The time evolution of the system and the associated expansion complicate the HBT interpretation and the temperature measurements.

Unfortunately, there is no unambiguous signal that validates if a phase transition and a formation of a Quark-Gluon Plasma has occurred. Most of the expected signals from a produced plasma can also be found in hadronic scenarios under certain conditions. Thus to conclude if a plasma has been produced in a collision, several signals have to be observed in the same event sample. A detailed discussion and description of the ideas behind some of the most promising signatures can be found in Ref. [5].

1.2 Nuclear Reactions and Collision Terminology

Particle accelerators are used to provide beams of atomic nuclei with velocities almost up to the speed of light. When these energetic particles collide with another atomic nucleus there is a nuclear reaction. This reaction may produce a system that allows to probe and study the fundamental properties and changes of nuclear matter. In order to create a system that undergoes a phase transition to a QGP, it is necessary to form the system with extremely high temperature and density. This can be achieved by colliding heavy nuclei at relativistic energies, where a large amount of the energy is deposited in a small volume of the system. Studies of fundamental properties of nuclear matter at or near its ground state are also performed using heavy-ion collisions. In this case the energies of the accelerated ions are non-relativistic, and range up till about 10% of the speed of light.

The collisions are induced by either steering the beam onto a stationary target (*fixed target* experiments) or by letting two beams coming from opposite directions cross each other (*collider* experiments). An advantage of collider experiments is that

all the beam energy is available for particle production, whereas in a fixed target experiment a large fraction of the energy is consumed by moving the center-of-mass. A fixed target experiment, however, allows for much easier focusing of the beam towards the stationary target compared to a collider experiment, which is very sensitive to the relative position of the two beams. The GASP03.12 and PHENIX experiments, which are described in chapter 2, represent a fixed target and a collider experiment, respectively. Both these experiments utilized heavy ion collisions transform the initial constituents into an excited system of nuclear matter. There are several different reaction meachanisms that may occur in such a collision, and depending on the beam energy and the centrality of the collision some mechanisms are more or less likely to occur. The sections below briefly describe the different reaction mechanisms, which dominate in the two experiments of the present thesis. In the GASP03.12 experiment a fusion-evaporation reaction is employed, whereas the relativistic collisions in PHENIX can be described using the spectator-participant model.

1.2.1 Fusion-Evaporation Reactions

The investigation of the properties of nuclear matter around its ground state requires a reaction mechanism that populates the nucleus of interest in an excited state. This can be achieved by a *fusion-evaporation reaction*, in which the nucleus is produced in an excited state with a certain angular momentum and excitation energy. The time evolution and the different stages of a fusion-evaporation reaction is schematically illustrated in Fig. 1.5 [7]. The incoming projectile collides with a target nucleus and the incident energy is shared among many of the involved nucleons. The projectile and target nuclei fuse together and form an excited and often rotating intermediate state referred to as a compound nucleus. The rotation frequency, and thus the angular momentum, of the compound nucleus depends on the collision centrality, which is characterized by the impact parameter, b, introduced in the participant-spectator model (cf. section 1.2.2).

Once the excited compound nucleus is formed there are many channels available for its decay. It may undergo fission or multi-fragmentation and thus split up into two or several constituents. Another possibility is that the highly excited compound nucleus decays through particle evaporation, in which light particles (protons, neutrons, and α particles) are emitted from the system. This allows the nuclear system to reduce its excitation energy and different residual nuclei are formed. At some stage the particle evaporation is hampered because the excitation energy of the system is not sufficient for yet another particle to be emitted. Instead the residual nucleus decreases in excitation energy via electromagnetic radiation and thus decay by emitting γ rays. Electromagnetic properties and radiation in nuclei is discussed further in section 4.1. The decay occurs at first through emission of statistical γ rays from the nuclear continuum and overgoes to emission of discrete γ rays until it reaches the ground state. These discrete γ rays carry information on the structure of the nucleus. They are detected in experiments and they allow the study of the properties of nuclear matter.

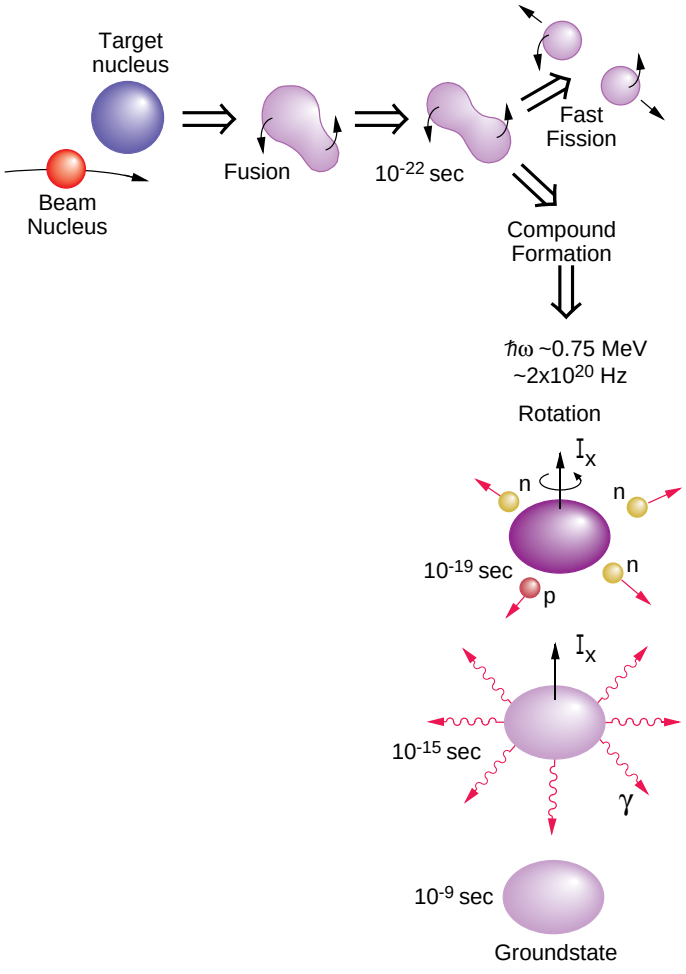

Figure 1.5: *Schematic illustration of the timescale in a nuclear fusion-evaporation reaction. Initially a target nucleus fuses together with an incoming beam nucleus and forms a nuclear compound system. The latter decays through particle evaporation and γ ray emission towards the ground state of the final nuclear product. Taken from Ref. [7].*

In the fusion-evaporation reactions emplyed in the present thesis the intermediate compound nucleus is extremely proton rich. Thus one would expect that most of the particles emitted in the evaporation process are protons or α-particles, which would create a residual nucleus located closer to the line of stability. However, due to the Coulomb barrier affecting the charge particles, the decay probability of neutron emission is still relatively high. This offers a possibility to study nuclei far from stability on the proton rich side of the nuclear chart. In such an experiment there will of course be several final residual nuclei, depending on the number of particles

evaporated. Examples of such reaction channels in a fusion-evaporation reaction are the two mirror nuclei ^{51}Fe and ^{51}Mn analysed in section 4.3.1. They were produced in a reaction using a ^{32}S beam colliding with a ^{24}Mg stationary target forming a ^{56}Ni compound nucleus. The reaction can be written as

$$^{32}\mathrm{S} \; + \; ^{24}\mathrm{Mg} \; \rightarrow \; ^{56}\mathrm{Ni}^{*} \; \rightarrow \begin{cases} ^{51}\mathrm{Mn} & + \quad 1\alpha 1\mathrm{p} \\ ^{51}\mathrm{Fe} & + \quad 1\alpha 1\mathrm{n} \end{cases} ,$$

where the * indicates the excited compund nucleus. It decays through particle emission and the two mirror nuclei can be found in the one-α-one-proton ($1\alpha 1$p) and one-α-one-neutron ($1\alpha 1$n) reaction channel, respectively. The decay continues as the two mirror nuclei emit γ rays, which are detected in the detector system and processed for further analysis.

1.2.2 The Spectator-Participant Model

In nucleus-nucleus collisions at relativistic energies, a hot and dense fireball of nuclear matter is produced and the collision geometry is described with the *spectator-participant model* [8], which is sketched in Fig. 1.6. In this picture the overlapping parts of the nuclei form a hot and dense region (participant region) while the remainders of the nuclei continues to move more or less undisturbed by the collision. The nucleons in the overlapping region are called the participants and the remaining nucleons are called spectators.

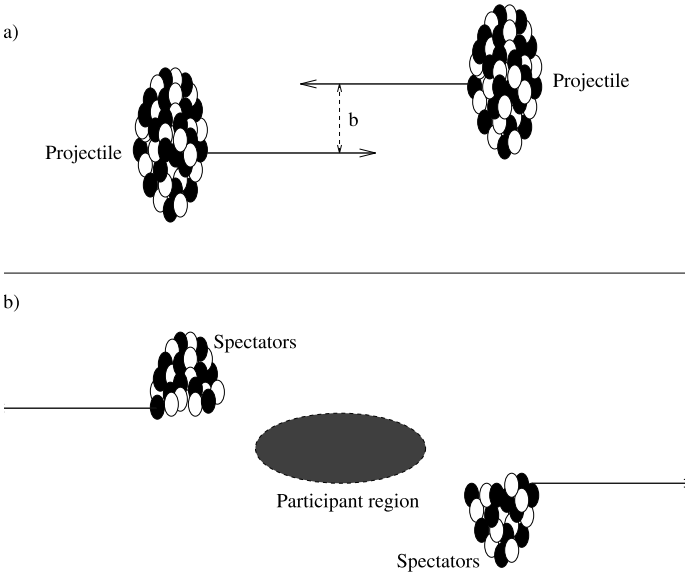

Figure 1.6: *Schematic illustration of the participant-spectator model in the centre-of-mass system. Panel (a) and (b) illustrates two heavy nuclei just before and after the collision, respectively.*

By introducing the impact parameter, b, the collision centrality can be quantified, which later is used to characterize the collisions in different event classes. The impact parameter is defined as the transverse distance between the centers of the two nuclei (see Fig. 1.6a) and values of b decide whether a collision is central[4] or peripheral[5]. It is not possible to directly measure the impact parameter in a collision and instead measurements of other quantities are used to determine the collision geometry. These quantities, for example, the number of produced particles and transverse energy, are strongly correlated to the number of participants in the collision, which allows to experimentally estimate the impact parameter. The energy transformed into particle production gives rise to a very high particle multiplicity, and it is possible to treat the system statistically. If one assumes that thermal equilibrium is reached, a thermodynamical model can be used to describe the system and thermodynamical variables (temperature, pressure etc.) may be calculated.

The momentum components, p_x, p_y, and p_z, of a particle are used to calculate quantities such as the transverse momentum, p_T, and the azimuthal angle, ϕ. The transverse momentum, which is the momentum component perpendicular to the beam direction, and the azimuthal angle are determined from the x and y components of the particle momentum as

$$p_T = \sqrt{p_x^2 + p_y^2} \tag{1.3}$$

and

$$\phi = \arctan \frac{p_y}{p_x}. \tag{1.4}$$

Using the transverse momentum the tranverse mass, m_T, is defined by

$$m_T = \sqrt{m_0^2 + p_T^2}, \tag{1.5}$$

where the speed of light is set to be unity and m_0 is the rest mass of the particle. The corresponding transformations to p_x, p_y, and p_z using the above quantities can be written as

$$\begin{aligned} p_x &= p_T \cdot \cos(\phi) \\ p_y &= p_T \cdot \sin(\phi) \\ p_z &= m_T \cdot \sinh(y) \end{aligned} \tag{1.6}$$

y is called the rapidity of the particle. It is measured along the beam direction and can be expressed in terms of the total energy of the particle and the longitudinal momentum component along the beam direction, p_z, as

$$y = \frac{1}{2} \ln \left(\frac{E + p_z}{E - p_z} \right). \tag{1.7}$$

An important feature of rapidity is that it is boost invariant and thus additive under a Lorentz transformation. This means that the shape of the rapidity distribution of particles from a moving source does not depend on the velocity of the source.

[4] b is close to zero

[5] b is slightly smaller than the sum of the two nuclei radii

Furthermore, the rapidity, in combination with the transverse mass, can be used to calculate the total energy, E, of a particle according to

$$E = m_T \cosh(y). \tag{1.8}$$

A frequently used approximation to the rapidity is the pseudorapidity, η, defined as

$$\eta = -\ln\left(\tan\frac{\theta}{2}\right), \tag{1.9}$$

where θ is the polar emission angle, i.e. the angle between the particle momentum $\vec{p}$ and the beam axis. The relation between the pseudorapidity and the rapidity is given by

$$\sinh\eta = \sinh(y) \cdot \frac{m_T}{p_T}, \tag{1.10}$$

where the transverse momentum and transverse mass are defined as in Eq. 1.3 and Eq. 1.5, respectively.

In heavy-ion collision terminology other important quantities are the invariant cross-sections. Using the above derived expressions the invariant differential cross-section of a particle can be written as

$$E \cdot \frac{d^3N}{dp_x dp_y dp_z} = \frac{d^3N}{p_T dy dp_T d\phi}, \tag{1.11}$$

where $dp_x dp_y dp_z = p_T m_T \cosh(y) \cdot dy dp_T d\phi$. From the right-hand side of Eq. 1.11 the invariance under Lorentz boosts along the beam axis is evident from the invariance of dy. The cross-section is normalized to the total number of events, N_{evt}. For an average over several events, there is azimuthal symmetry and thus no ϕ dependence. Hence, the invariant cross-section can be written as

$$\frac{d^2N}{2\pi N_{evt} p_T dy dp_T}. \tag{1.12}$$

This work is partly based on measurements of invariant cross-section for deuterons and anti-deuterons at relativistic energies using the PHENIX detector. The data analysis of these measurements are presented in chapter 3.

Chapter 2

Experiments

The properties of nuclear matter can be studied in data obtained from experiments utilizing nucleus-nucleus collisions. To detect and probe the constituents and the evolution of such collisions requires advanced detector technology, which is often developed and constructed within world wide collaborations. The size and economical cost of a detector system is strongly correlated to the physical motivation for the experiment. The smaller constituents that are to be probed the larger and more complex detector systems are required.

The present thesis employ four experiments: GASP03.12 performed at Legnaro National Laboratory (LNL), GSFMA73 performed at Argonne National Laboratory (ANL), GS2k017 performed at Lawrence Berkley National Laboratory (LBNL), and the PHENIX experiment performed at the Relativistic Heavy Ion Collider (RHIC) at Brookhaven National Laboratory (BNL). In particular, the thesis is based on data from the GASP03.12 and the PHENIX experiment.

2.1 The GASP03.12 Experiment

The GASP03.12 experiment was performed at LNL in collaboration with five European institutes[1]. The primary goal was to determine effective charges in the fp shell via lifetime measurements in the mass $A = 51$ mirror nuclei ^{51}Fe and ^{51}Mn. The experiment utilized a heavy-ion fusion evaporation reaction with a ^{32}S beam at 95 MeV on a fixed ^{24}Mg target. The produced γ rays were detected in the GASP spectrometer [9], which was used in combination with the Cologne plunger device [10] to perform the lifetime measurements.

2.1.1 Detectors and Experimental Set-Up

GASP (GAmma-ray SPectrometer) comprises 40 Hyper-Pure Germanium (HPGe) detectors with anti-Compton shields and a 4π calorimeter of 80 BGO[2] crystals. The detectors are divided in two hemispheres, which are closed to a sphere during the

[1] Participants from Lund, Cologne, Keele, Padova, and Legnaro.

[2] $Bi_4Ge_3O_{12}$

experiment. One such hemisphere is shown in Fig. 2.1. The figure shows the experimental set-up for the GASP03.12 experiment using the Cologne plunger device, BGO inner ball, and the HPGe detectors.

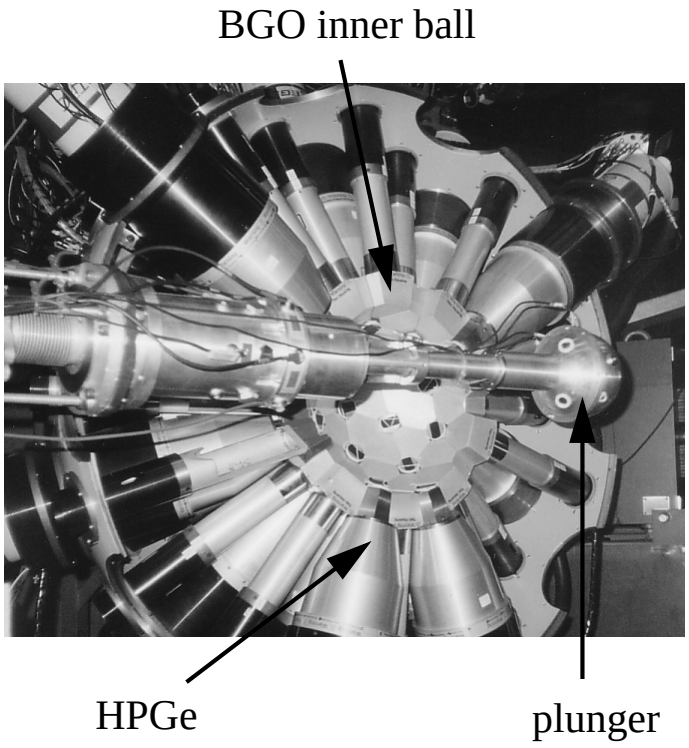

Figure 2.1: *One hemisphere of the GASP detector array with the Cologne plunger device, BGO inner ball, and the HPGe detectors. The beam enters from the left.*

The HPGe detectors are placed 27 cm from the target position and distributed in eleven rings ranging from 31.7° to 148.3° relative to the beam axis. In the offline analysis some of the detector rings are combined, which results in seven rings situated at average angels of 34.6°, 59.4°, 72.0°, 90.0°, 108.0°, 120.6° and 145.4°. The configuration of GASP including the BGO inner ball corresponds to a total photo peak efficiency of about 3% at 1332 keV. However, the efficiency almost doubles to 5.8% if the BGO inner ball is removed and the HPGe detectors are positioned closer to the target. This second configuration is utilized in experimental situations where the most important feature is the total efficiency. In the GASP03.12 experiment the GASP detector array was used in its standard configuration with both the HPGe detectors and the BGO inner ball.

The BGO elements surrounding the HPGe detectors work as anti-Compton shields. They are used as veto detectors to perform suppression of the background arising from Compton scattering. If a γ ray is Compton scattered out of the HPGe detector only a fraction of its energy is recorded and the event should be neglected. The scattered

γ ray can be detected in the surrounding BGO material, which allows to veto such events and thus suppress the background. However, it is possible that a γ ray deposits all its energy in the HPGe detector and at the same time a second γ ray is detected in a BGO crystal, which vetoes the event. Such a scenario, which happens more frequently for events with large γ ray multiplicity, is prevented by the cover of the front of the surrounding BGO material with Heavimet absorbers, which should make sure that the BGO shield only fires on scattered radiation from the HPGe detectors.

Ancillary detector systems

Additional detector systems can be used in conjunction with the GASP array in order to obtain cleaner spectra, which may, for example, offer a possibility to identify γ ray transitions of a specific residual nucleus. A few of the standard systems available at LNL are:

- **ISIS**: A detector array of 40 silicon $\Delta E - E$ telescopes used to detect light charged particles produced in the reactions.
- **N-Ring**: A neutron detector array consisting of six individual detectors, which replaces the 6 most forward elements of the BGO inner ball.
- **CAMEL**: A Recoil Mass Separator placed downstream in the target hall.

However, none of the above ancillary detector systems were used in the GASP03.12 experiment set-up. Instead the lifetime measurements were performed using the Cologne plunger device (see Fig. 2.1), which replaced the standard target chamber and was connected directly to the beam line. It consists of a small reaction chamber in which a target and a stopper foil are placed. The holder for the stopper foil is mobile that allows to vary the target-stopper distance, which is the basic requirement for the present lifetime analysis. In section 2.1.2 the principle of the lifetime measurements are discussed in more detail. During the experiment the target-stopper distance was varied over 21 distances, which in the offline analysis is combined into nine effective distances.

Data Handling

The produced signals from the BGO crystals and the HPGe detectors are fed into the GASP Data Acquisition System (DAQ), which allows to set an event trigger. For the current experiment events with at least one BGO crystal and two HPGe detectors firing in coincidence were accepted by the trigger. The signals for an accepted event were sampled and processed further and eventually stored on disk. The stored data was used in the offline analysis to extract the lifetimes of the analogue $27/2^-$ states in the $A = 51$ mirror pair.

2.1.2 Lifetime Measurements

Nuclear lifetimes of excited states range from more than 10^{15} years to below 10^{-20} s for very short-lived states. Therefore, a variety of different lifetime measurement techniques exist. The most straight forward technique is to use electronic modules

(e.g. Time-to-Amplitude-Converter) to extract nuclear lifetime in coincidence measurements of the respective radiation. This method, however, is limited to the time resolution of the detector system and can be used for $\tau > 1$ ns. Lifetimes in the picosecond region can be determined using Doppler-shift methods, which is the focus of the present thesis. In particular, it employs the Recoil Distance Doppler Shift method in the analysis of the GASP03.12 experiment.

Recoil Distance Doppler Shift Technique (RDDS)

The RDDS method is a standard technique to measure lifetimes of excited states in the picosecond region. Using a plunger device, the recoiling nuclei from a thin target foil are stopped at different distances in a stopper foil. Hence, γ rays are emitted either during the flight of the recoils or when the recoils are stopped in the stopper. The principle is illustrated as in Fig. 2.2. The energy of γ rays emitted in flight, γ_F,

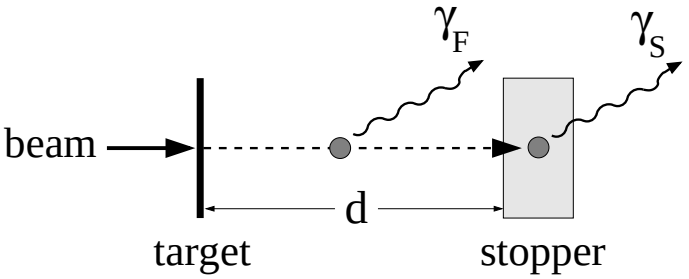

Figure 2.2: *Schematic view of the plunger principle where produced recoils in a thin target foil are stopped in a stopper. Changing the target-stopper distance, d, changes the relative intensites of decays in flight, $I_{\gamma,F}$, and at rest, $I_{\gamma,S}$.*

is subject to a Doppler shift while the energy of γ rays emitted from the stopper, γ_S, is unshifted. Thus, detecting γ rays at an angle θ, with respect to the recoil direction, allows to distinguish between γ_F and γ_S. The intensity of the transition de-populating an excited nuclear state is therefore distributed in a flight peak and a stopped peak, I_F and I_S, respectively. These intensities are given by

$$I_F = I_0(1 - e^{-t/\tau}) \qquad \text{and} \qquad I_S = I_0 e^{-t/\tau}. \tag{2.1}$$

Here, τ is the lifetime of the excited state and $t = d/v_r$ is the flight time corresponding to the target-stopper distance, d, and the recoil velocity, v_r. The fraction of the γ ray intensity in the stopped components, $F(t)$, shows an exponential dependence as

$$F(t) \equiv \frac{I_S}{I_S + I_F} = e^{-t/\tau}, \tag{2.2}$$

which gives the lifetime of the excited nuclear state.

In the above derivation it is assumed that the excited state is populated promptly, i.e., the state is not fed through upper levels that also have finite lifetimes. In such a case the determined lifetime will correspond to an effective lifetime of the excited

state. Thus, such feedings need to be accounted for, which can be done by least square fittting of the experimental data to several exponentials. Another method, developed to account for this problem, is the Differential Decay Curve Method [11, 12].

Differential Decay Curve Method (DDCM)

The DDCM technique also employs intensities of flight and stopped components of the transitions to derive the lifetime of an excited state. Consider two γ rays emitted in a nuclear decay sequence as illustrated in Fig. 2.3. τ_1 and τ_2 are the corresponding lifetimes for the two states. The intensity of the flight and stopped component for the

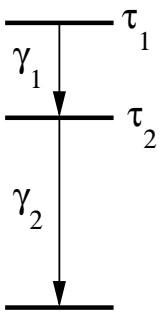

Figure 2.3: *Illustration of γ ray decay of two excited states with lifetime τ_1 and τ_2, respectively.*

first transition are I_{F1} and I_{S1}, respectively, which allows to derive the corresponding intensities for the second transition as

$$I_{F2} = I_{F1}(1 - e^{-t/\tau_2}) \qquad \text{and} \qquad I_{S2} = I_{F1}e^{-t/\tau_2} + I_{S1}. \tag{2.3}$$

The I_{F2} and I_{S2} intensities are measured for γ rays in coincidence with the flight component of the first transition. Therefore, $I_{S1} = 0$ in Eq. 2.3 and the lifetime of the second excited state is given by

$$\tau_2 = \frac{I_{S2}}{\dot{I}_{F2}}, \tag{2.4}$$

where $\dot{I}_{F2}$ is the first order derivative of the intensity for the flight component. Using this method allows to determine the lifetime from the observed coincidence intensities for each of the target-stopper distances. Furthermore, the use of coincidences eliminates any contributions of possible side-feeding and thus gives the real lifetime of the nuclear state.

The present thesis attempted to employ the DDCM method in the analysis of the ^{53}Fe nucleus (cf. section 4.3.2). The determined intensities of the flight and stopped components are used as input parameters to the NAPATAU[3] software [13]. This software performs fits of the given input parameters and provides all computing necessary to extract the lifetime of interest. However, it was found that the lifetime

[3]DDCM analysis software, which has been developed at the University of Cologne

of the states of interest cannot be determined using this software with the provided intensities. Due to the small amount of statistics and the difficulties with background subtraction, in particularly for the flight components, it was impossible to obtain good fits. Instead, the standard RDDS technique was utilized.

2.2 The GSFMA73 and GS2k017 Experiments

The GSFMA73 and GS2k017 experiments were performed under nearly identical conditions. Both experiments utilize a ^{32}S $+^{28}$ Si fusion-evaporation reaction with a 130 MeV ^{32}S beam. The detector set-up consisted of the Gammasphere array [14] for detection of the emitted γ rays, the 4π CsI-array Microball [15] for detection of evaporated charge particles and the Neutron Shell [16] to detect neutrons. The event trigger was set to accept events with at least four detected γ rays or one neutron and at least three detected γ rays. Recorded raw data was processed through various offline analysis packages as described in section 4.3. More details on the experimental conditions and set-up can be found in, for example, Ref. [3, 17].

2.3 The PHENIX Experiment

The PHENIX experiment [18, 19] has been designed to investigate nuclear matter created in ultra-relativistic nuclear collisions. It is one of four[4] large detector systems operating at the Relativistic Heavy Ion Collider, which accelerates beams of nuclei ranging from protons to gold. The detector system is divided into several subsystems, which are constructed, maintained, and developed by a world wide collaboration consisting of about 500 physicists and engineers.

The primary goal of PHENIX is to detect signs of the Quark-Gluon Plasma and to characterize its physical properties. Hence, PHENIX offers to probe the nuclear system at different stages of its evolution, i.e., from the initial collision to the final hadronization. Many quantities related to proposed QGP signatures can be studied. For instance, the initial stages of the collision can be characterized by measuring direct photons and lepton pairs whereas information of the freeze-out is probed by looking at, for example, coalescence probabilities of various nuclei and anti-nuclei.

This thesis presents an analysis on light nuclei (deuterons and anti-deuterons) produced at RHIC during its second year of running. The analysis is based on data from PHENIX and a detailed description is found in chapter 3.

2.3.1 Detector Arrangements and Data Acquisition

The PHENIX detector consists of two central spectrometer arms (East and West), two muon spectrometers (North and South), and three global detector systems. A sketch of the experimental layout, as of the second year of running, is shown in Fig. 2.4. A brief description of the design and functionality of the different subsystems is given below.

[4]The others being BRAHMS, PHOBOS, and STAR

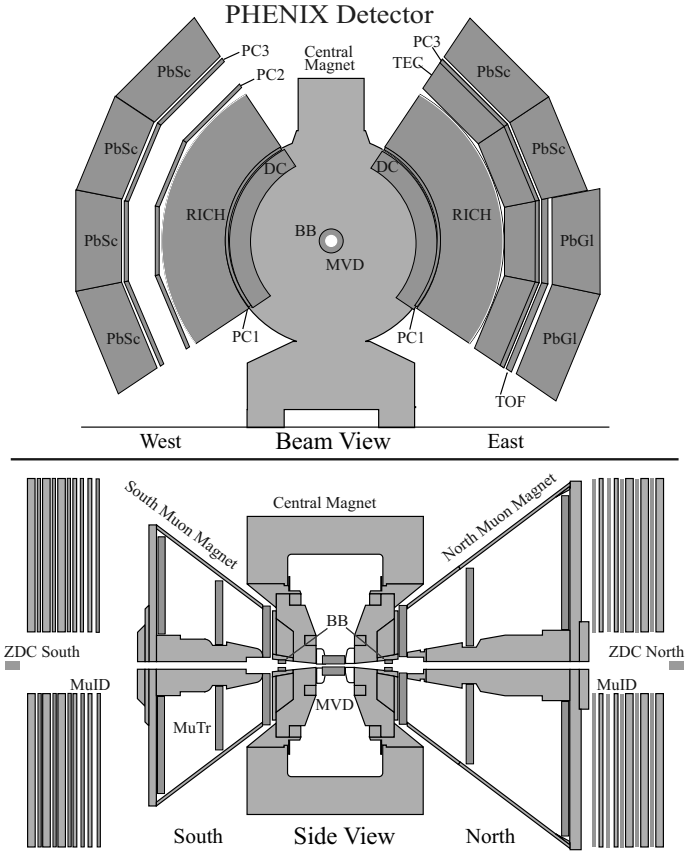

Figure 2.4: *The experimental layout of the PHENIX detector for 2002, viewed along the beam axis (top) and from the side (bottom).*

Central Arm Spectrometers

The central arm spectrometers (Fig. 2.4) are designed to perform momentum measurements, charge particle tracking, identification of various particle species, and to measure photon and electron energies. It covers the pseudorapidity interval $\Delta\eta = \pm 0.35$ and is divided into two arms (East and West), each with an azimuthal (ϕ) coverage of 90°. The spectrometer arms surround a **Central Magnet** that provides an axial field parallel to the beam. The particle tracking is performed using three detector systems;

- **Drift Chambers** (DC): Perform high resolution p_T measurements and provide precise tracking of charged particles traversing the spectrometers.
- **Pad Chambers** (PC): Pixel-based multi-wire proportional chambers that perform space coordinate measurements for charged particle trajectories. Described in more detail in section 2.3.2.

- **Time Expansion Chamber** (TEC): Provides tracking in the $r - \phi$ plane and improves the momentum resolution for high p_T particles. It measures the energy deposition (dE/dx) along the tracks, which contributes to electron-pion separation.

The primary particle identification, energy measurements, and flight-time measurements are carried out with other subsystems:

- **Ring Imaging CHerenkov** (RICH): The primary detectors for electron identification, which provides good electron-pion discrimination.
- **Time-Of-Flight** (TOF): Performs high-resolution flight-time measurements (time resolution around 80 ps) used for particle identification of charged hadrons.
- **ElectroMagnetic Calorimeters** (PbSc/PbGl): Provide photon identification and perform measurements of particle energy and flight time. The calorimeter is divided into two sectors of lead-glass (PbGl) Cherenkov calorimeters and six sectors of lead-scintillator (PbSc) sampling calorimeters.

Muon Spectrometers

To detect dimuons emerging from vector meson decay (J/Ψ, Ψ', Υ etc.) PHENIX has designed two forward muon spectrometers, which detect muons with full azimuthal acceptance. Each consist of a

- **Muon Tracker** (MuTr): Consists of multi-plane drift chambers for high precision particle tracking.
- **Muon Identifier** (MuId): Composed of alternating layers of steel absorbers and low resolution tracking chambers. This combination provides a discrimination of pions, since they are stopped in the steel absorbers.

Each spectrometer is supplied with a radial magnetic field from the **Muon Magnets**.

Detectors for Global Observation

Important properties of the collision (centrality, collision vertex position etc.) are carried out by three different detector systems placed close to the beam axis:

- **Zero-Degree Calorimeters** (ZDC): Measure the energy deposited from spectator neutrons emitted along the beam direction. They serves as a centrality trigger and can be used to monitor luminosity and to determine the position of the collision vertex.
- **Multiplicity Vertex Detector** (MVD): Provides measurements of collision vertex position and event multiplicity. It has not been fully operational during the two first years of data taking.
- **Beam-Beam Counters** (BBC): Composed of an array of Cherenkov counters arranged in a cluster around the beam pipe. The BBC produce a signal for the primary interaction trigger but are also used to determine the collision vertex position and provide the start time for time-of-flight measurements.

In the offline analysis, the combined information from the BBC and the ZDC is used to determine the collision centrality, which is used for event selection.

Data Handling

The detector signals are sampled and recorded with Front-End-Modules (FEM), which store signals in analogue or digital memories. At every beam crossing some detectors produce data used as input for the level-1 trigger (LVL1). If the trigger is accepted data in the FEM are transmitted by optical fibers to Data Collection Modules (DCM). To minimize the dead time, the Data Acquisition system (DAQ) can buffer five accepted LVL1 events, which allows the DAQ system to continously record and transfer signals. The accepted data fragments are processed in the DCM to perform zero suppression, error checking, and data reformatting. The output is sent to an Event Builder (EvB), where the final stage of the event assembly takes place. The EvB provides an environment for the level-2 trigger (LVL2), which can further enrich the sample of accepted events. Finally, the data are recorded to disk for storage.

The raw data files are used as input to a reconstruction chain producing Data Summary Tapes (DST), which contain a variety of information; global event characteristics (vertex position), individual particle properties (momenta, charge), particle hit coordinates (x, y and z) for a specific detector, etc. The reconstruction occurs within an offline framework, where information from different subsystems is combined to reconstruct, for example, particle tracks or particle momenta. The DST are processed through a second offline framework to reduce redundant information. The new format, the so-called microDST, is used for various physics analyse.

2.3.2 The Pad Chambers

The central arm spectrometers comprise three different layers of pad chambers located at radial distances 2.5 m (PC1), 4.2 m (PC2), and 4.9 m (PC3) from the beam axis. They cover around ± 0.35 units of pseudorapidity and 90° in azimuth angle in each spectrometer arm. Each detector is a pixel-based multi-wire proportional chamber, has a very high detection efficiency, and is designed to fulfill the following roles:

- Provide reliable track information with accurate coordinates in the beam direction and good position resolution in the other directions.
- Provide redundancy for the drift chamber measurements.
- Define entry and exit coordinates of the particle identification subsystems.
- Provide fast position information to be used in the LVL2 trigger.

Readout and Performance of the Chambers

To achieve good spatial resolution, high detection efficiency, and reliable pattern recognition the chambers are constructed as multi-wire proportinal chambers with one cathode plane finely segmented in small pads. The signals are read out by readout cards placed directly on the backplane of a chamber. Each card handles a group of 48 different pads. To reduce the number of readout channels, each pad is segmented in nine rectangular copper electrodes, so-called pixels. The pixel-pads are arranged in an interleaved pattern as illustrated in Fig. 2.5. The size of the pixels are chosen to collect an equal amount of charge on each pixel, hence the center pixels, which are located above the anode wires, are designed somewhat smaller. One center pixel and

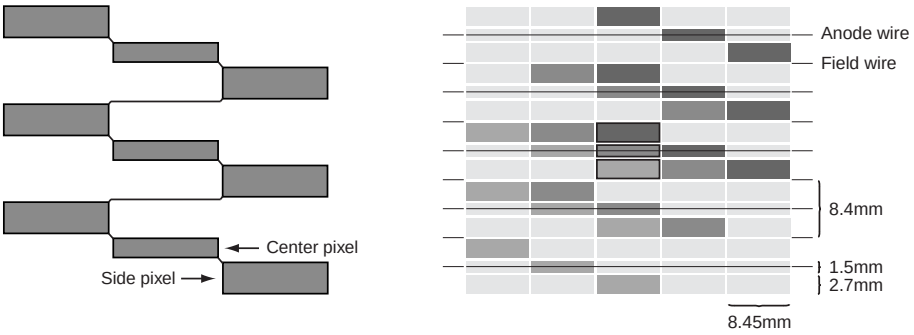

Figure 2.5: *A pad consists of nine pixels (left). The pixel layout showing three fired pads combined to form one fired cell (right). Values are for PC1.*

two side pixels, from different but adjacent pads, are used in conjunction to form a cell. A valid hit in a cell, and thus the detector chamber, is obtained if all three pads corresponding to a cell fires in coincidence. An individual pad fires if the collected charge exceed a pre-set discriminator threshold. The pixel pattern gives each cell a unique set of pad numbers and thus the location of the fired cell can be determined.

Before installation, each pad chamber type was tested extensively with cosmic rays to verify the charge gain on the anode wires and investigate the efficiency and position resolution. The experimental set-up and measurements are described in more detail in section 6 of PAPER I. An estimate of the charge gain on the anode wires was made for one pad chamber of each type. The chambers had no wire readout installed, but for a few wires the signal was extracted and the pulse height distribution was recorded on a multichannel analyzer. The charge gain was determined by dividing the charge corresponding to the peak with the number of electrons liberated by a minimum ionizating particle. For the used gas mixture (50% ethane and 50% argon) this was calculated to be 95 electrons/cm using tabulated values for the average energy needed to liberate an electron-ion pair [20].

The operating voltage was chosen on the basis of the different measurements and the values were set to 1700 V for PC1, 1840 V for PC2 and 1880 V for PC3, which gives a high efficiency and the voltages are safely below the onset of sparking.

Chapter 3

Deuteron and anti-deuteron physics with PHENIX

In high-energy heavy-ion experiments the measurements of hadronic spectra provide valuable information about the final freeze-out of the system. Such measurements have been performed utilizing the PHENIX detector at RHIC during its second year of operation. Analysis of light nuclei, in particular deuterons and anti-deuterons, produced in $\sqrt{s_{NN}} = 200$ GeV Au+Au collisions is presented in the sections below. This analysis is one of two independent searches for deuterons and anti-deuterons within the PHENIX collaboration. The two analyses have been processed in parallel with slightly different approaches and the difference was used for the estimation of systematic errors. The combined results of the two analyses can be found in PAPER II.

Deuterons may arise as fragments from the remaining beam nuclei, but the possibility for these fragments to survive into the central region is negligible at RHIC. Instead the observed deuterons and anti-deuterons must have been formed by either direct production of deuteron/anti-deuteron pairs or more likely by coalescence of nucleon pairs. To describe the production mechanism of the deuterons and anti-deuterons, a coalescence model is introduced.

3.1 The Coalescence Model

In the coalescence model [21, 22] a deuteron (anti-deuteron) is formed if a proton (anti-proton) and a neutron (anti-neutron) are close enough in both momentum and configuration space to fuse together. Assuming that neutrons and protons have the same momentum distributions, the invariant deuteron (anti-deuteron) cross-section in the coalescence model is related to the primordial nucleon cross-sections by

$$E_d \cdot \frac{d^3 n_d}{{dp_d}^3} = B_2 \left(E_p \cdot \frac{d^3 n_p}{{dp_p}^3} \right)^2 , \tag{3.1}$$

where $p_d = 2p_p$. B_2 is the coalescence parameter, which reflects the volume of the particle-emitting source. Thus, the coalescence parameter can be determined via the ratio of the yield of deuterons and the yield of protons squared.

Consider a distribution of protons and neutrons within a nuclear volume, V, as sketched in Fig. 3.1.

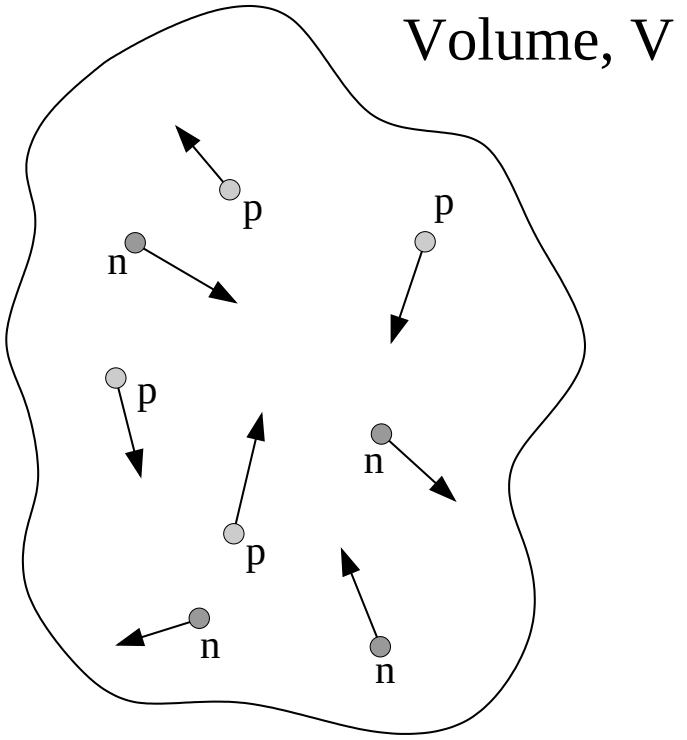

Figure 3.1: *Protons and neutrons distributed over a small volume, V.*

The distribution function in phase space is defined as

$$f(\vec{r},\vec{p}) = \frac{d^6 n_p}{dp_x dp_y dp_z dx dy dz} \cdot (2\pi\hbar)^3, \tag{3.2}$$

where dn is the number of particles in a small cell ($dp_x dp_y dp_z dx dy dz$) centered around a point ($p_x,\ p_y,\ p_z,\ x,\ y,\ z$) in phase space. Assuming that protons and neutrons are uniformly distributed within the volume V, the distribution function can be written

$$f(\vec{r},\vec{p}) = \frac{d^3 n}{dp^3} \cdot \frac{(2\pi\hbar)^3}{V}. \tag{3.3}$$

The two nucleons are supposed to bind together and form a deuteron by coalescence. In such a scenario, the deuteron density can be expressed with the distribution function (Eq. 3.3) of protons and neutrons as

$$\frac{1}{2s_d+1}\left(\frac{d^3 n_d}{{dp_d}^3}\cdot\frac{(2\pi\hbar)^3}{V}\right) = \frac{1}{2s_p+1}\left(\frac{d^3 n_p}{{dp_p}^3}\cdot\frac{(2\pi\hbar)^3}{V}\right)\frac{1}{2s_n+1}\left(\frac{d^3 n_n}{{dp_n}^3}\cdot\frac{(2\pi\hbar)^3}{V}\right),$$

where s_d,, s_p, and s_n are the spins of the deuteron, proton, and neutron, respectively [23]. The resulting deuteron momentum, p_d, is the sum of the proton and

neutron momentum, i.e., $p_d = p_p + p_n \approx 2p_p$. Assuming the same momentum distribution for the two nucleons, i.e., $\frac{d^3n_p}{dp_p{}^3} = \frac{d^3n_n}{dp_n{}^3}$, the deuteron density can be expressed as

$$\frac{d^3n_d}{dp_d{}^3} = \frac{3}{4}\frac{(2\pi\hbar)^3}{V} \cdot \left(\frac{d^3n_p}{dp_p{}^3}\right)^2, \tag{3.4}$$

which can be related to the invariant deuteron yield by

$$E_d \cdot \frac{d^3n_d}{dp_d^3} = \frac{E_d}{E_p{}^2} \cdot \frac{3}{4}\frac{(2\pi\hbar)^3}{V} \cdot \left(E_p \cdot \frac{d^3n_p}{dp_p{}^3}\right)^2. \tag{3.5}$$

By comparing Eq. 3.1 with Eq. 3.5 it is seen that the coalescence parameter can be written as

$$B_2 = \frac{E_d}{E_p^2} \cdot \frac{3}{4}\frac{(2\pi\hbar)^3}{V}, \tag{3.6}$$

which can be used to estimate the volume of the source. In a simple model, where one assumes that the protons and neutrons are uniformly distributed over a spherical volume with radius R and where p_T is small ($p_T < m$), the relation between B_2 and R is given by

$$B_2 \approx \frac{m_d}{m_p^2} \cdot \frac{9}{2}\frac{\pi^2}{c^2}\frac{\hbar^3}{R^3} \tag{3.7}$$

3.2 Data Analysis

A study of deuteron and anti-deuteron production in Au+Au collisions at RHIC has been performed using data from the PHENIX experiment. Data was taken during the second year of running at $\sqrt{s_{NN}} = 200$ GeV with most of the detector subsystems in operation. To identify deuterons and anti-deuterons, the following detector systems in the east central tracking arm were used:

- Drift Chamber (DC)
- Two layers of Pad Chambers (PC1 and PC3)
- Time-of-Flight detector (TOF)

In addition, information from the Beam-Beam Counters (BBC) and Zero-Degree Calorimeters (ZDC) were used for triggering and event selection. The total event sample consists of about 20 million minimum bias events, where each event is required to have a vertex of $|z_{vertex}| < 20$ cm from the nominal crossing point.

Below is a description of the analysis work providing the event and track selection cuts, particle identification, correction simulations, and some results.

Event and track selection cuts

Deuterons (anti-deuterons) were identified with the particle-identification capabilities of the central tracking arm through the flight time measured with the TOF. Due to the low yield of deuterons (anti-deuterons) compared with other hadrons, stricter cuts on the tracks were required to be able to extract and determine a clear signal.

A first selection of tracks was done by requiring a drift chamber track to have an associated hit in the first layer of pad chambers (PC1). In order to define further cuts and investigate how these affect the signal, only a fraction ($\approx$ 3 million minimum bias events) of the total event sample was used. These cuts are described below and once determined they were applied to the full data sample in order to extract the signal of the deuterons (anti-deuterons).

TOF Association

As the particle identification was performed using the TOF wall, the first restriction on the event sample was to include only events with a recorded hit in the TOF detector. To reduce the number of wrongly reconstructed particle trajectories a momentum dependent track selection cut, $F_{TOF}(p_T)$, was introduced. This was derived from calculating the distance, R, between the the intercept of the projected track with the TOF wall (x_{TRK}, y_{TRK}, z_{TRK}) and the position of the associated TOF hit (x_{TOF}, y_{TOF}, z_{TOF}), determined by the TOF itself. The distance was calculated for different p_T-bins in the interval $0.4 < p_T < 5.0$ GeV/c. Figure 3.2 shows the distribution of R for $1.0 < p_T < 1.1$ GeV/c. The distribution for each bin was fitted

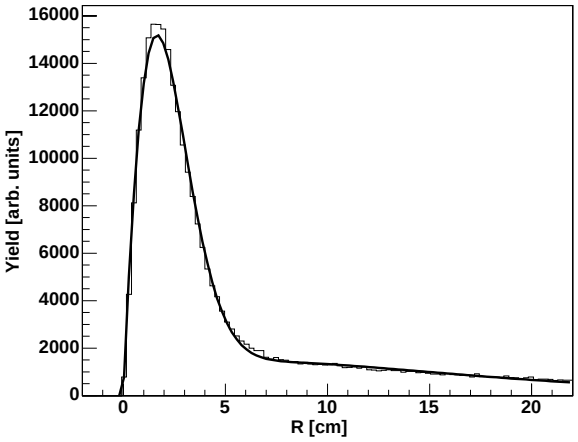

Figure 3.2: *Distribution of R for tracks with* $1.0 < p_T < 1.1$ *GeV/c fitted with a function f(R) as described in the text.*

with a function $f(R)$ written as

$$f(R) = A \cdot R \cdot e^{-B\left(R+C\cdot R^2\right)} + D \cdot R \cdot e^{-E\cdot R}. \tag{3.8}$$

The first term represents the peak of extrapolated tracks that are correctly associated to a TOF hit whereas the second term correspond to the background arising from wrongly associated tracks. The track selection cut was set for each momentum interval such that the signal equals half the background. This allows to derive $F_{TOF}(p_T)$. Only tracks with $R \leq F_{TOF}(p_T)$ were accepted in the final analysis.

PC3 Association

Utilizing the two layers of pad chambers in the east arm spectrometer (PC1 and PC3) allows to extrapolate the particle trajectory to the primary vertex. The z coordinate of the extrapolated track (z_{pc_vertex}) was compared with the event z vertex (z_{vertex}) from the BBC, which provides a cut associated with PC3.

Constructing a straight line with the pad chamber coordinates (x_{PC1}, y_{PC1}, z_{PC1} and x_{PC3}, y_{PC3}, z_{PC3}), the z_{pc_vertex} is calculated by extrapolating the line to $r = 0$, where $r = \sqrt{x^2 + y^2}$, i.e.,

$$z_{pc\_vertex} = \frac{z_{PC1} \cdot \sqrt{x_{PC3}^2 + y_{PC3}^2} - {}_{PC3} \cdot \sqrt{x_{PC1}^2 + y_{PC1}^2}}{\sqrt{x_{PC3}^2 + y_{PC3}^2} - \sqrt{x_{PC1}^2 + y_{PC1}^2}}. \tag{3.9}$$

The difference between the two vertices ($\Delta z_{vertex} = z_{pc\_vertex} - z_{vertex}$) was calculated and plotted for a set of different p_T-bins in the range $0.4 < p_T < 5.0$ GeV/c. The distribution for each bin was fitted to the sum of two gaussians that corresponds to the peak of the distribution and the background, respectively. This allows to derive a momentum dependent selection cut, $F_{PC3}(p_T)$, which was set at 2σ of the gaussian equivalent to the signal. Only tracks with $\Delta z_{vertex} \leq F_{PC3}(p_T)$ were used in the final analysis.

Energy loss

The measured energy loss in the TOF wall, ΔE, was used to introduce an energy loss cut, ΔE_{cut}, which was parameterized as

$$\Delta E_{cut} = \frac{A}{\beta^2} + B, \tag{3.10}$$

where β is the particle velocity. The parameters A and B were determined from a scatter plot of the energy loss measured in the TOF vs. $1/\beta^2$. To simplify the selection of the parameters the expected mean energy loss was calculated according to the Bethe-Bloch formula [24]

$$-\frac{dE}{dx} = K \cdot \rho \cdot \frac{Z}{A} \cdot \frac{z^2}{\beta^2} \left[2 \cdot \ln \left(\frac{2 m_e c^2 (\beta\gamma)^2}{I^2} \right) - 2\beta^2 \right] \tag{3.11}$$

using $K = 0.1535$ MeVcm^2/g, $z = 1$ for a singly charged particle, and the electron mass $m_e c^2 = 511$ keV. The values for the absorbing material in the TOF were $\rho = 1$ g/cm^3, $\frac{Z}{A} = 0.5$, and $I = 64.7$ eV with a thickness of $dx = 1.5$ cm. With the expected mean energy loss included in the scatter plot, the parameters were set to generate a lower limit. Hence, only tracks with $\Delta E \geq \Delta E_{cut}$ were used in the final analysis.

Effect of applying the cuts

The effect of consecutively applying the different cuts to reduce the background in the deuteron mass spectrum is illustrated in Fig. 3.3. Mass spectra are obtained using the drift chamber information in conjuction with information from the TOF wall as described in section 3.2. Figure 3.3a shows the obtained mass spectrum for all

drift chamber tracks associated with a hit in the first layer of pad chambers (PC1). Panel b, c, and d illustrates the improvement of the mass spectrum after applying each of the described cuts by first applying the TOF association (b) followed by the PC3 association (c) and finally the energy loss cut (d). It is seen that the signal-to-background ratio improves to about 2:1 after the final cuts have been applied.

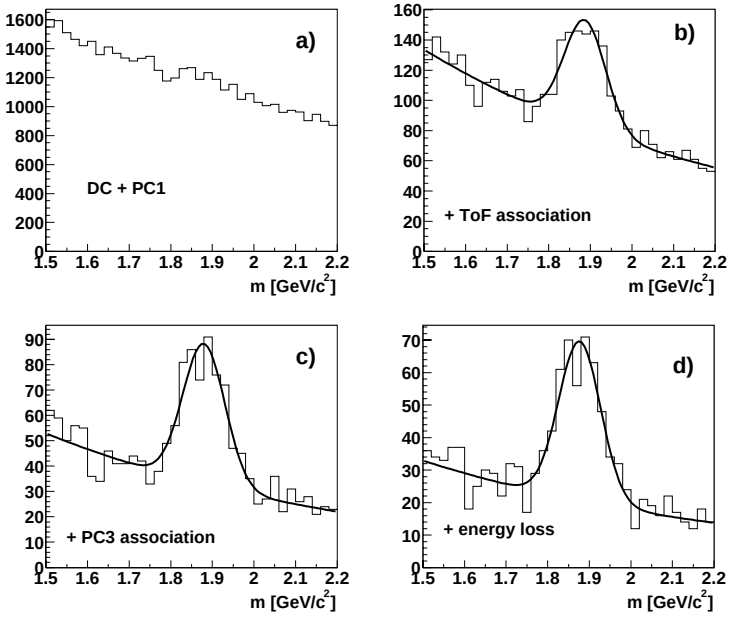

Figure 3.3: *Reconstructed mass spectra for deuterons after consecutively applying different track quality cuts as described in the text. The background is clearly reduced after the final cuts have been applied. The signal-to-background ratio improves to about 2:1. The solid curves show fits to data.*

Particle Identification and Raw Yields

The cuts described in the previous section are applied to the total event sample and tracks surviving the cuts are used in the analysis. Flight times measured in the TOF are used in combination with flight lengths and reconstructed momenta to obtain mass spectra and to identify particles. An illustration of the excellent particle identification capabilities of the tracking system is shown in Fig. 3.4. Plotted is $q \cdot (1 - \beta)$ as a function of $1/p$, where $\beta = v/c$, p is the total reconstructed momentum, and q is the charge in elementary units. Bands of pions (π^+, π^-), kaons (K^+, K^-), protons (p), anti-protons ($\bar{p}$), deuterons, and anti-deuterons are clearly seen in the figure.

The mass, m, of a particle is calculated from the reconstructed momentum, p, and

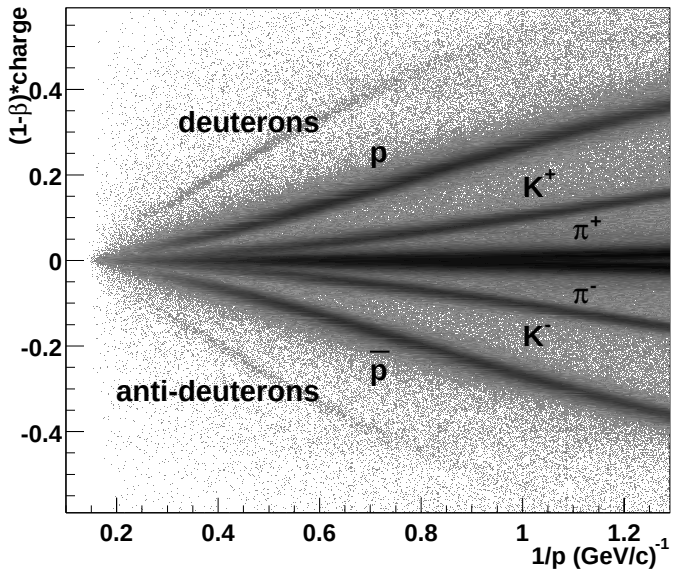

Figure 3.4: *Illustration of the excellent particle identification capabilities from time-of-flight measurements. Bands of different particle species are marked.*

the flight time, t, measured by the TOF according to

$$m = \frac{p}{c} \cdot \sqrt{\left(\frac{tc}{L}\right)^2 - 1}, \tag{3.12}$$

where L the flight length. To extract the yield of deuterons and anti-deuterons, the mass spectra were constructed for different bins in p_T. The distributions were fitted to a gaussian with an exponential background as

$$f(M_{fit}) = Cbe^{-bm} + \frac{N}{\sqrt{2\pi}\sigma} \cdot e^{-\frac{(m-M_{fit})^2}{2\sigma^2}}, \tag{3.13}$$

where b, C, N, M_{fit}, and σ are free parameters. N gives the yield of deuterons (anti-deuterons) in the momentum bin, M_{fit} is the fitted mass, and σ is the width of the mass distribution. The values of M_{fit} and the extracted raw yields, N_{RAW} for the different p_T-bins are listed in Table 3.1.

Table 3.1: *Extracted values of the raw yields and masses for deuterons and anti-deuterons for different p_T-bins. The tabulated mass of a deuteron is 1875.6 MeV/c^2.*

	deuterons		anti-deuterons	
p_T [Gev/c]	N_{RAW}	M_{fit} [MeV/c^2]	N_{RAW}	M_{fit} [MeV/c^2]
1.0-1.5	1065.8±79.7	1868±4	472.7±49.0	1862±5
1.5-2.0	1046.3±46.3	1864±2	518.1±35.9	1860±3
2.0-2.5	750.4±37.1	1872±2	382.2±30.1	1856±4
2.5-3.0	404.1±30.6	1884±4	186.8±25.2	1861±8
3.0-3.5	172.4±24.6	1877±8	54.8±12.4	1845±7

Corrections and simulations

The corrections needed to convert the raw particle yield to the normalized invariant distributions are obtained from simulations. Simulated events are processed through a GEANT-based Monte Carlo simulation package developed for PHENIX (PISA). This simulations package includes particle decay (if applicable), multiple Coulomb scattering, hadronic and electromagnetic interactions, and the acceptance, efficiency, and resolution of the detector. A shortcoming of GEANT is that no hadronic interactions of deuterons or anti-deuterons are implemented. Thus, the performed single-particle corrections do not account for this effect, and the corrections for hadronic interactions have been studied separately. This is discussed below.

The multiplicity dependent part of the efficiency corrections has been investigated by embedding simulated particles in real events and checking whether it gets reconstructed or not. This investigation was performed by other members within the PHENIX collaboration.

Single-particle corrections

Single-particle corrections were done using two event samples, each comprising one million events with one particle type (deuteron or anti-deuteron) per event. The particles were generated with a flat distribution in rapidity covering the full azimuthal angle ($0 \leq \phi \leq 360°$) and with $0.5 \leq p_T \leq 8.0$ GeV/c. The events were processed through PISA and the correction factors (C) were were obtained by comparing the number of reconstructed deuterons (N_{rec}) in a given p_T-bin with the number of generated deuterons (N_{gen}) in the same bin. The correction factors used to convert the raw yields were calculated for the same p_T-bins as for the data. The numbers are listed in Table 3.2.

Hadronic Interaction

Since hadronic processes for nuclei are not implemented in GEANT, stand-alone calculations are performed to determine the corrections for the hadronic interactions of deuterons and anti-deuterons. The calculations are based on the accessible detector material, which a particle encounters while traversing from the primary vertex position to the TOF wall. From the path lengths, l_i, and densities, n_i, of the different

Table 3.2: *Correction factors for deuterons and anti-deuterons. The error given for C is the statistical error.*

	deuterons			anti-deuterons		
p_T [Gev/c]	N_{gen}	N_{rec}	C	N_{gen}	N_{rec}	C
1.0 - 1.5	66408	724	91.7±3.4	66306	774	85.7±3.1
1.5 - 2.0	46765	646	72.4±2.9	46852	671	69.8±2.7
2.0 - 2.5	40048	651	61.5±2.4	39680	680	58.4±2.2
2.5 - 3.0	37265	639	58.3±2.3	37287	691	54.0±2.1
3.0 - 3.5	36288	693	52.4±2.0	36388	687	53.0±2.0

materials the probability that a particle should survive without suffering any hadronic interaction is calculated as

$$exp(-\sum_i \sigma_i n_i l_i), \tag{3.14}$$

where σ_i are the corresponding cross sections. The inelastic cross section for deuteron and anti-deuteron induced interactions is parameterized using the proton (neutron) and anti-proton (anti-neutron) cross sections. This parameterization is discussed in Appendix A.

Using the parameterization, the hadronic interaction probabilities are calculated for (anti-)protons and (anti-)deuterons. The calculations for (anti-)protons are compared with the interaction probabilities obtained from GEANT simulations, which indicated similar results. Hence, the mean of the methods is used as the final nucleon interaction probabilities, and the difference gives an estimate of the systematic error.

Finally, the hadronic interaction probabilities for deuterons and anti-deuterons are determined using the ratio of the interaction probabilities of (anti-)deuterons to those of (anti-)protons. The ratios are applied to the final nucleon interaction probabilities, which gives the interaction probabilities $\approx 10.0(15)\%$ and $\approx 15.0(35)\%$ for deuterons and anti-deuterons, respectively.

Secondary deuterons

Deuterons can be produced in secondary (knock-out) reactions between the produced particles and the surrounding detector material or the beam pipes. This background source is investigated using an event sample of around one thousand central HIJING events. The simulated events, which contained no primary deuterons, are fed through PISA and the output is analysed as follows:

The particles detected in the TOF wall are identified and all deuterons are selected. Since the event sample contained no primary deuterons, the detected deuterons must have been produced in secondary reactions. From the particle kinematics, a secondary vertex position and the momentum distribution of the deuterons is calculated. It was found that a large fraction of the secondary deuterons were produced in the TOF wall itself. These are, however, not to be considered as a problem as they are not reconstructed as deuterons within the reconstruction code. Instead, the investigation focuses on secondary deuterons produced close to the primary vertex. This is achieved by only selecting particles with a secondary vertex $|x| < 20$ cm and $|y| < 20$ cm.

The yields of selected secondary deuterons are calculated for different bins in p_T. The obtained p_T distribution is normalized to the number of events and extrapolated to higher momenta, which provide a comparison with normalized raw data yields. The result is illustrated in Fig. 3.5. However, the simulations utilized only central

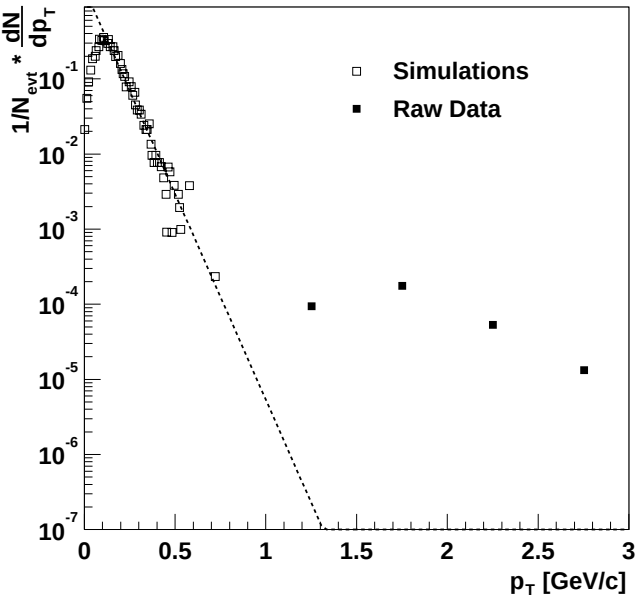

Figure 3.5: *Secondary deuterons from simulated events compared to extracted raw yields in data. The dashed line shows an extrapolation of simulated data to higher p_T.*

events with a full coverage of the azimuthal angle, ϕ, whereas the raw data yields are extracted for minimum bias events using the TOF acceptance in ϕ. These factors will increase the relative relation between the simulations and the measured data. Therefore, it can be concluded that secondary deuterons are negligible for $p_T > 1.0$, which is the lower limit for the first measured data point.

The production of secondary anti-deuterons can be neglected as any detected anti-deuteron must have been produced in the primary collision.

3.3 Physics Results

Following the analysis procedure described above, this section presents some physics results obtained using an event sample of 19.3 million minimum bias events. These results are combined with those of the second (anti-)deuteron analysis performed within the PHENIX collaboration, and the summarized results are presented in PAPER II.

The invariant yields of deuterons and anti-deuterons are extracted from the measured raw yields by applying the corrections discussed in the previous section. For the present results, however, there are no multiplicity dependent corrections included. The invariant yield, normalized to the number of events, N_{evt}, can be written as

$$\frac{d^2N}{2\pi N_{evt} p_T dy dp_T}, \tag{3.15}$$

where the dy dependence is included in the single-particle corrections, dp_T are the widths of the used p_T-bins and the value of p_T is equal to the center of each p_T-bin, respectively. The values of the normalized yields are listed in Table 3.3. The

Table 3.3: *Normalized invariant yields of deuterons and anti-deuterons.*

	deuterons	anti-deuterons
p_T [GeV/c]	$d^2N/2\pi p_T dy dp_T$ $[\mathrm{GeV/c}]^{-2}$	$d^2N/2\pi p_T dy dp_T$ $[\mathrm{GeV/c}]^{-2}$
1.0 - 1.5	$(1.19\pm0.10)\cdot10^{-3}$	$(5.23\pm0.57)\cdot10^{-4}$
1.5 - 2.0	$(6.61\pm0.37)\cdot10^{-4}$	$(3.34\pm0.26)\cdot10^{-4}$
2.0 - 2.5	$(3.13\pm0.19)\cdot10^{-4}$	$(1.60\pm0.14)\cdot10^{-4}$
2.5 - 3.0	$(1.31\pm0.11)\cdot10^{-4}$	$(5.92\pm0.82)\cdot10^{-5}$
3.0 - 3.5	$(4.24\pm0.62)\cdot10^{-5}$	$(1.44\pm0.33)\cdot10^{-5}$

invariant spectra are fitted by an exponential in m_T, which allows to determine the temperature parameter, T, as the inverse slopes. Using the extracted fit parameters the spectra are extrapolated to lower and higher transverse momentum. Figure 3.6 shows the exponential fits to the spectra, including the extrapolation. The fits give temperature parameters of $T = 463(16)$ MeV and $T = 442(19)$ MeV for deuterons and anti-deuterons, respectively.

The extrapolation of the fits can be used to calculate the rapidity density, dN/dy, and the mean transverse momenta, $\langle p_T \rangle$. The rapidity density is calculated by integrating the (anti-)deuteron yields over p_T as

$$\frac{dN}{dy} = 2\pi \int_0^\infty p_T f(p_T) dp_T, \tag{3.16}$$

where $f(p_T)$ is the invariant yield as a function of p_T expressed as

$$f(p_T) = \frac{d^2N}{2\pi p_T dy dp_T}. \tag{3.17}$$

In a similar manner, $\langle p_T \rangle$ is calculated as the ratio of two integrals as

$$\langle p_T \rangle = \frac{\int_0^\infty {p_T}^2 f(p_T) dp_T}{\int_0^\infty p_T f(p_T) dp_T} \tag{3.18}$$

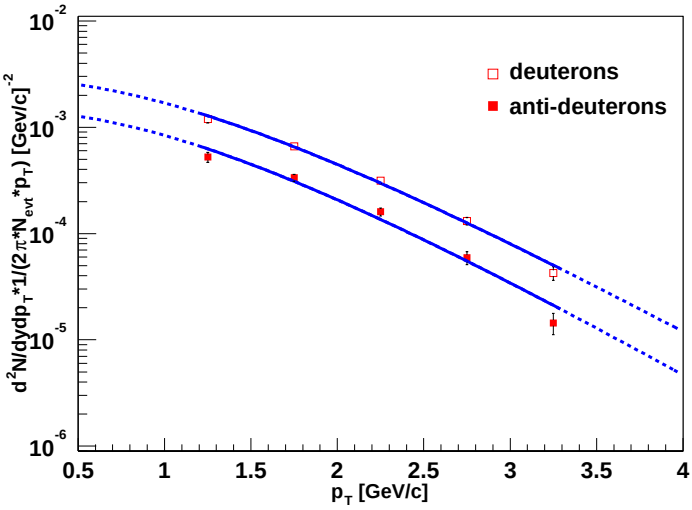

Figure 3.6: *Exponential fits in p_t and m_T to the normalized invariant deuteron and anti-deuteron spectra. Dashed lines show the extrapolation of the fits.*

Using the fitted function in m_T, the values of dN/dy and $\langle p_T \rangle$ were calculated as described above. The result is presented in Table 3.4.

Table 3.4: *Values of dN/dy and $\langle p_T \rangle$ for deuterons and anti-deuterons.*

	dN/dy	$\langle p_T \rangle$ [GeV/c]
deuterons	0.0200(6)	1.41(4)
anti-deuterons	0.0090(3)	1.37(5)

The centrality dependence of the invariant p_T-spectra is investigated by dividing the minimum bias events into different centrality classes. For each centrality class, the raw yields are extracted and converted to normalized yields. The final yields are compared and it is concluded that the yield of deuterons and anti-deuterons increases with centrality.

The Coalescence parameter (B_2)

As discussed in section 3.1, the invariant (anti-)deuteron yields can be related to the invariant (anti-)proton yields with the coalescence parameter, B_2, as

$$B_2 = \frac{E_d \cdot \frac{d^3 n_d}{dp_d{}^3}}{\left(E_p \cdot \frac{d^3 n_p}{dp_p{}^3}\right)^2}, \tag{3.19}$$

where $p_d = 2p_p$. Thus, the B_2 value is calculated taking the ratio of the invariant (anti-)deuteron spectra to the square of the invariant (anti-)proton spectra. However, (anti-)protons produced from weak decays, e.g., Λ ($\bar{\Lambda}$), have to be taken into account in the study of the coalescence parameter. The Λ ($\bar{\Lambda}$) has a lifetime that corresponds to a few cm. Hence, (anti)-protons from such decays will not contribute in the coalescence of a (anti-)deuteron. Therefore, the utilized (anti-)proton spectrum need to be corrected for this feed-down effect, which will lead to a substantial increase in the coalescence parameter. The final analysis employ feed-down corrected spectra. However, at the time of the present investigation no feed-down corrections had been applied to the (anti-)proton spectra.

The study of the coalescence parameter employs the extracted invariant deuteron (anti-deuteron) spectrum and the proton (anti-proton) spectra obtained from another PHENIX analysis [25]. Figure 3.7 shows the coalescence parameter as a function of transverse momentum. The coalescence parameter increases with transverse momen-

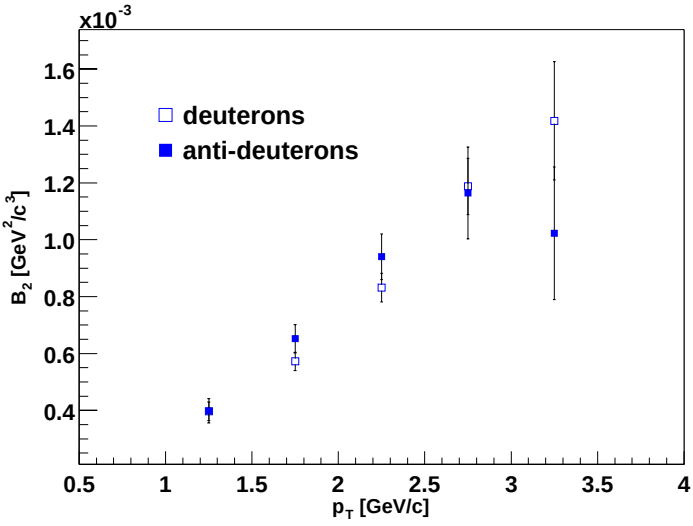

Figure 3.7: *Coalescence parameter as a function of transverse momentum for deuterons (anti-deuterons). Note that the employed proton (anti-proton) spectra are not corrected for the feed-down effect.*

tum, which can be seen as a sign of collective transverse expansion [26]. It is known that the p_T-dependence of B_2 is related to the density profile as well as the expansion velocity of the source. Assuming that the nucleons before freeze-out are uniformly distributed within a (static) sphere with radius R, B_2 can be related to R according to Eq. 3.7. The increase of B_2 with p_T is inconsistent with such a simple model and indicates a decreasing source size with increasing p_T. This is in qualitative agreement with results from HBT and indicates an expanding source.

Chapter 4

Gamma-Ray Spectroscopy

Measurements of discrete γ rays, emitted from the late stages in a heavy-ion fusion-evaporation reaction, allow to study the properties of atomic nuclei in their ground states and excited states. In particular, gamma-ray spectroscopy offers a possibility to probe electromagnetic properties that can be predicted from various theoretical models. Hence, from comparison between experimental data and theoretical calculations conclusions on fundamental effects in nuclei can be drawn.

Lifetimes of excited states and related electromagnetic properties have been determined from the analysis of data from the GASP03.12 experiment. Comparison with large-scale shell-model calculations provide valuable information on core polarization effects and a quantitative estimate of effective transition operators.

4.1 Electromagnetic Properties

The description of electromagnetic properties in nuclei is covered in many text books on nuclear physics, for example Ref. [27, 28, 29]. Hence, this section only discuss briefly some of the topics relevant for the present thesis.

The classical theory of radiation fields are transfered into the quantum domain through replacement of the classical multipole moments with appropriate multipole operators, $\mathcal{M}(\sigma L)$. These operators describe the change of a nucleus from its initial state, ψ_i, to its final state, ψ_f. The character of the radiation field, which can be of either electric or magnetic nature, is denoted σ and the multipole order of the radiation is denoted L. An electromagnetic transition with a multipole of order L carries an angular momentum of $L\hbar$ per photon[1].

Consider a multipole transition from an initial excited nuclear state to a final nuclear state, $\psi_i \rightarrow \psi_f$. The properties of the states are described in terms of angular momentum $\vec{J}_i$, $\vec{J}_f$ and parity π_i, π_f. In the γ-ray transition, the photon is emitted with an angular momentum $\vec{L}$ such as to conserve angular momentum

$$\vec{J}_i = \vec{J}_f + \vec{L}. \tag{4.1}$$

[1]Such as $L = 1$ for a dipole transition, $L = 2$ for a quadrupole transition, and so on.

Hence, the angular momentum selection rules for a γ decay can be written

$$|J_i - J_f| \leq L \leq J_i + J_f \qquad (\text{no } L = 0), \tag{4.2}$$

where L is the multipolarity of the transition. A given transition thus comprises a mixture of several components where the lowest permitted multipole transition usually dominates. Monopole γ-ray transitions ($L = 0$) are forbidden because a photon has an intrinsic angular momentum of $1\hbar$. Thus no γ decay can occur for $0^{\pi_i} \rightarrow 0^{\pi_f}$ transitions. Instead, these transitions proceed through internal conversion, in which the excitation energy is released by ejecting an electron in an atomic orbital.

The character of the radiation field is determined by the relative parity of the nuclear states in combination with the multipolarity. The parity selection rules for the character of the multipole transition are

$$\begin{array}{lcll} \pi_i & \neq & \pi_f & L \text{ odd} \rightarrow \text{electric},\ L \text{ even} \rightarrow \text{magnetic}, \\ \pi_i & = & \pi_f & L \text{ even} \rightarrow \text{electric},\ L \text{ odd} \rightarrow \text{magnetic}. \end{array} \tag{4.3}$$

The transition probability, $\lambda(\sigma L)$, for γ-ray emission of multipolarity L and character σ is expressed by

$$\lambda(\sigma L, J_i \rightarrow J_f) = \frac{8\pi(L+1)}{\hbar L[(2L+1)!!]^2} \left(\frac{E_\gamma}{\hbar c}\right)^{2L+1} B(\sigma L, J_i \rightarrow J_f), \tag{4.4}$$

where the quantity $B(\sigma L)$ is the so-called reduced transition probability. Note that the transition probability depends on the γ-ray energy, E_γ, while the reduced transition probability contains no energy dependence. $B(\sigma L)$ can be expressed as

$$B(\sigma L, J_i \rightarrow J_f) = \frac{1}{2J_i + 1} |\langle \psi_f || \mathcal{M}(\sigma L) || \psi_i \rangle|^2, \tag{4.5}$$

in which $\langle \psi_f || \mathcal{M}(\sigma L) || \psi_i \rangle$ is the reduced matrix element. For a nucleus with A nucleons the multipole operator become the sum over all single particle operators. The electric and magnetic operators are written as

$$\mathcal{M}(EL) = \sum_{i=1}^{A} e_i r_i^L Y_{Lm_L}, \tag{4.6}$$

$$\mathcal{M}(ML) = \sum_{i=1}^{A} \mu_N \left(\frac{2}{L+1} g_l^i l_i + g_s^i s_i\right) \cdot [\nabla (r_i^L Y_{Lm_L})], \tag{4.7}$$

where r_i is the orbital radius for particle i and Y_{Lm_L} is the corresponding spherical harmonic function [27]. The single-particle operators are derived for a particle with charge e_i and a magnetic moment determined by the gyromagnetic factors g_l^i and g_s^i. For free nucleons the g-factors are found empirically to be $g_l^p = 1$, $g_l^n = 0$ and $g_s^p = 5.59$, $g_s^n = -3.83$ for protons and neutrons, respectively.

For a γ decay, $\psi_i \rightarrow \psi_f$, the lifetime of the initial state, τ_i, can be written as

$$\tau_i = \frac{1}{\lambda_{tot}(J_i \rightarrow J_f)}, \tag{4.8}$$

where λ_{tot} is the total transition probability given as a sum over all possible multipole components:

$$\lambda_{tot}(J_i \rightarrow J_f) = \sum_{j,k} \lambda(\sigma_j L_k, J_i \rightarrow J_f). \tag{4.9}$$

In most cases, however, the lowest multipole order dominate the transition and the contribution from other components can be neglected. A common exception are mixed $E2/M1$ transitions. The degree of mixing between the two lowest multipolarity components is given by the mixing ratio

$$\delta(\sigma_2 L_2/\sigma_1 L_1) = \sqrt{\frac{\lambda(\sigma_2 L_2)}{\lambda(\sigma_1 L_1)}}. \tag{4.10}$$

The γ decay of an excited nuclear state has so far been considered to take place via a γ-ray transition into one final state. However, in many cases the depopulation of the initial state can occur via several branches into different final states. The total transition rate, of course, would be the sum of the individual transition probabilities. The contribution of each transition to the sum is determined by the branching ratio, b_r, which is the relative transition probability written as

$$b_r = \frac{\lambda_{tot}(\sigma L)}{\lambda_{TOT}}, \tag{4.11}$$

where $\lambda_{tot}(\sigma L)$ is the total transition rate for one of the γ-ray transitions and λ_{TOT} is the total transition rate for all transitions.

From experimentally determined lifetimes the reduced transition probabilities for the multipole transitions to the final states can be determined using Eq. 4.4 if the corresponding branching ratio and any possible mixing of different multipole components are known. The reduced transition probability for an electric quadrupole transition, for example, can be determined from experimental data via

$$B(E2; J_i \rightarrow J_i - 2) = b_r \cdot \frac{816.2}{\tau_i E_\gamma^5}, \tag{4.12}$$

where τ_i is the lifetime of the initial state in ps, and E_γ the energy of the transition in MeV.

The number of nucleons that participate in the transition is related to the configuration of the relevant nuclear states. In the extreme single-particle case, where only one nucleon contributes to the transition, Weisskopf gives estimates of the reduced transition probabilities as

$$B^W(EL) = \frac{1}{4\pi}\left(\frac{3}{L+3}\right)^2 (1.2A^{1/3})^{2L}, \tag{4.13}$$

$$B^W(ML) = \frac{10}{\pi}\left(\frac{3}{L+2}\right)^2 (1.2A^{1/3})^{2L-2}, \tag{4.14}$$

where $B^W(EL)$ and $B^W(ML)$ are expressed in the units $e^2\mathrm{fm}^{2L}$ and $\mu_n^2\mathrm{fm}^{2L-2}$, respectively [27]. Using these relations, the Weisskopf estimates for the lifetime of an initial nuclear state can be determined for the extreme case of a pure single-particle transition. They are illustrated in Fig. 4.1.

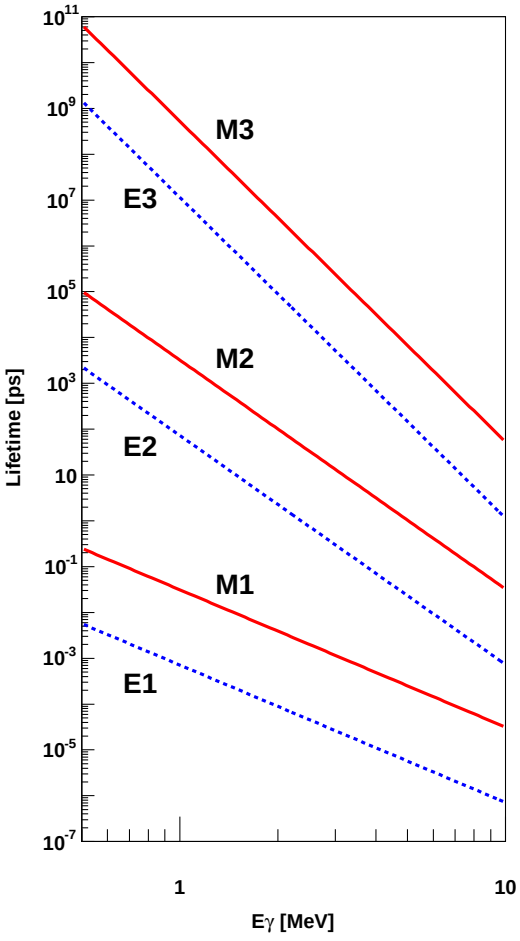

Figure 4.1: *Lifetime of an excited state as a function of the transition energy to the final state. Different lines correspond to different multipolarity and character of the emitted γ ray.*

The Weisskopf estimate for the excited $27/2^-$ states in the $A = 51$ mirror nuclei can be derived. The excited states decays via an $E2$ transition with energy of $E_\gamma = 777$ keV and $E_\gamma = 704$ keV for ^{51}Fe and ^{51}Mn, respectively. The corresponding Weisskopf estimates for the lifetimes are determined to be $\tau_{Fe} = 257$ ps and $\tau_{Mn} = 418$ ps. However, the measured lifetimes are much smaller (cf. section 4.3.1) than the Weisskopf estimates and consequently $B(E2)_{exp} > B^W(E2)$. If the experimentally measured values are much greater than the Weisskopf estimates it may indicate that the transition is of collective nature.

Reduced transition probabilities can be estimated from theoretical models accord-

ing to Eq. 4.5, in which the transition operators given in Eq. 4.6 and Eq. 4.7 are employed. The models cannot, however, treat the full many-body quantum problem of a given nucleus with A nucleons. Therefore, in shell-model calculations one defines an inert core and thus limits the calculations to the remaining valence nucleons, which are restricted to move only in a given number of valence shells. The valence nucleons involved in the transition are assumed to be independent of the nuclear core. This, however, may not be valid, since they may polarize and couple to the core. The polarization effect can be compared to the tidal waves caused on the surface of the earth by the orbiting moon. Figure 4.2 illustrates the effect for a single nucleon outside a spherical core.

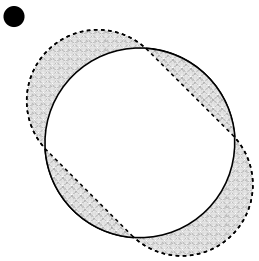

Figure 4.2: *Illustration of how a single nucleon located outside a spherical core polarizes the core.*

To account for such core polarization effects, the empirical g-factors and the bare nucleon charges are replaced in the calculations with effective g-factors and effective nucleon charges.

Effective Charges

We thus introduce an effective charge for the protons, ε_p, and neutrons, ε_n, respectively. For a nucleon i, the single-particle electric quadrupole operator becomes (cf. Eq. 4.6)

$$\mathcal{M}(E2) = \varepsilon_i r_i^2 Y_{20}, \tag{4.15}$$

where ε_i denote the introduced effective nucleon charge. The reduced $E2$-transition probabilities are now written as the sum over all particles according to (cf. Eq. 4.5)

$$B(E2; J_i \to J_f) = \frac{1}{2J_i + 1} |\langle J_f || \sum_{i=1}^{A} \varepsilon_i r_i^2 Y_{20} || J_i \rangle|^2. \tag{4.16}$$

In the harmonic oscillator $\langle r^2 \rangle$ is given by

$$\langle r^2 \rangle = \frac{\hbar}{m\omega} \left(N + \frac{3}{2} \right) = b_0^2 A^{1/3} \left(N + \frac{3}{2} \right), \tag{4.17}$$

where N is the harmonic oscillator principle quantum number. In large-scale shell-model calculations, using harmonic oscillator wave functions, the parameter b_0 is commonly set to $b_0 = 1.01$ [30, 31]. Changing b_0 thus provides an easy way to vary the nucleon radius in the calculations.

The effective charges contain the bare charges plus a contribution from the polarization, e_{pol}. When the particle is bound in a harmonic oscillator potential the polarization charge is expressed as (cf. Ref. [27])

$$e_{pol} = \frac{Z}{A}e, \tag{4.18}$$

which gives effective nucleon charges $\varepsilon_p = 1.5\ e$ and $\varepsilon_n = 0.5\ e$ for protons and neutrons, respectively, in the case of $N = Z$ nuclei. However, here no distinction is made between protons and neutrons.

The polarization charge consists of an isoscalar, $e_{pol}^{(0)}$, and an isovector, $e_{pol}^{(1)}$, component such that

$$e_{pol} = e_{pol}^{(0)} + e_{pol}^{(1)} \cdot 2t_z, \tag{4.19}$$

where $t_z = -1/2$ and $t_z = +1/2$ corresponds to the proton and neutron, respectively. Accordingly, the effective proton and effective neutron charges can be written as

$$\begin{aligned} \varepsilon_p &= 1 + e_{pol}^{(0)} - e_{pol}^{(1)}, \\ \varepsilon_n &= e_{pol}^{(0)} + e_{pol}^{(1)}. \end{aligned} \tag{4.20}$$

Thus a single neutron will polarize the charged core more strongly than a single proton (cf. Ref. [27]).

The isoscalar and isovector components of the polarization charge arise from the coupling of the valence nucleons to the corresponding modes of the so-called giant quadrupole resonance (GQR), which is an excited vibrational state of the core. Depending on the relative phase of the oscillation of the protons and neutrons an isoscalar or an isovector mode of the GQR is generated. In the isoscalar mode the protons and

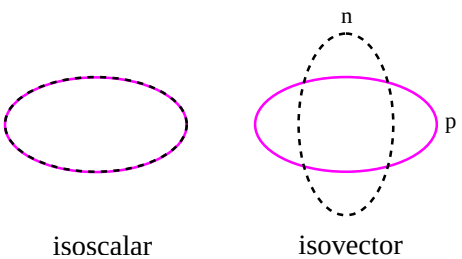

Figure 4.3: *Illustration of isoscalar (left) and isovector (right) giant quadrupole resonance modes. Protons (solid) and neutrons (dashed) are oscillating in phase and out of phase, respectively.*

neutrons oscillates with the same phase, and in the isovector mode they are out of phase [29]. The two different modes are sketched in Fig. 4.3.

According to Bohr and Mottelson [29] the total polarization charge can be written as

$$e_{pol} = e\left(\frac{Z}{A} - 0.32\frac{N-Z}{A} + \left(0.32 - 0.3\frac{N-Z}{A}\right)\cdot 2t_z\right), \tag{4.21}$$

where the isoscalar and isovector components thus are given as

$$\begin{aligned} e_{pol}^{(0)} &= e\left(\tfrac{Z}{A} - 0.32\tfrac{N-Z}{A}\right), \\ e_{pol}^{(1)} &= e\left(0.32 - 0.3\tfrac{N-Z}{A}\right). \end{aligned} \tag{4.22}$$

The corresponding isoscalar and isovector components of the polarization charge for a $N = Z$ nucleus are $e_{pol}^{(0)} = 0.5\ e$ and $e_{pol}^{(1)} = 0.32\ e$. The effective nucleon charges along the $N = Z$ line are thus expected to be $\varepsilon_p = 1.18\ e$ and $\varepsilon_n = 0.82\ e$ for protons and neutrons, respectively.

It is of general interest to determine the effective nucleon charges from experimental data to perform comparisons with theoretical estimations. From this it may be possible to draw conclusion of, for example, the dependency on the polarization charges in terms of isospin or the number of valence particles. A detailed description of an unique study of the $A = 51$ mirror pair, where a quantitative measurement of effective charges is performed, can be found in section 4.3.1.

4.2 Mirror nuclei

Effective nucleon charges are introduced to nuclear models to account for core polarization effects. To probe and determine effective charges experimentally are not only an interesting but also a quite challenging task. One way to access and pin down the effective charges are detailed studies of so called mirror nuclei, which are pairs of nuclei with the number of protons and neutrons interchanged. The observed differences between the two mirror nuclei are expected to arise mainly from the Coulomb force, which directly affects only the positively charged protons. If this force is neglected, the properties of the two mirror nuclei are expected to be identical as the protons and neutrons can be treated as two different quantum states of the same particle, the nucleon. In this picture an isospin quantum number, t, is introduced to describe the nucleon wave function, which allows to distinguish a proton from a neutron. A single nucleon has $t = 1/2$ with two possible directions in isospin space, $t_z = -1/2$ and $t_z = +1/2$, for the proton and neutron, respectively. For a system of several nucleons the total isospin quantum number, T, can enact all values in steps of one such as

$$\frac{1}{2}|N - Z| \leq T \leq \frac{1}{2}(N + Z) \tag{4.23}$$

where N and Z are the number of neutrons and protons, respectively. The projection of the total isospin, T_z, is the sum of the projections of the individual nucleons. Thus for a many-nucleon system T_z can be written as

$$T_z = \frac{1}{2}(N - Z) \tag{4.24}$$

where mirror nuclei are described as a, for example, $T_z = \pm 1/2$ mirror pair. An example of a $T_z = \pm 1/2$ mirror pair are the $A = 51$ nuclei. ^{51}Fe has 26 protons and 25 neutrons, while ^{51}Mn has 25 protons and 26 neutrons.

The nuclear force affecting the nucleons inside the nucleus can to first order be described with a two-body interaction. The possible combinations that arise are *pp*, *nn*, or *pn* interactions, where *p* represent the proton and *n* the neutron. In a two-nucleon system the possible total isospin is either $T = 1$ or $T = 0$, which correspond to an isospin triplet state (containing a *pp*, *pn*, or *nn* pair) and an isospin singlet state (containing a *pn* pair), respectively. It has been found that the *pp* interaction is very nearly the same as the *nn* interaction under the assumption that the Coulomb force is neglected. Also the interaction of a *pn* pair, in the same isospin state as the *pp* or *nn* pair ($T = 1$), is equal to that of the *pp* and *nn* pair. The *pn* pair may also be found in an isospin state ($T = 0$) that has no counterpart in the *pp* or *nn* system, because it is forbidden due to the Pauli exclusion principle. In such an isospin state the *pn* interaction is found to be stronger than that of the *pp* or *nn* pairs. The equality of the *pp*, *nn*, and, *pn* interactions in the $T = 1$ isospin state is known as charge independence of the nuclear force. With charge symmetry of the nuclear force is meant that only the *pp* and *nn* interactions are the same.

The dependency of the nuclear force may be studied using excited states in mirror nuclei, which are expected to reveal identical energy level structures assuming isospin symmetry and charge independence. However, the isospin symmetry is certainly broken by the Coulomb interaction between protons, and thus small differences in the level structure are expected. Furthermore, also (small) violations of the charge symmetry and the charge independence of the nuclear force give rise to fluctuations in the energy level structures. These effects can be investigated by looking at energy differences of "mirror states" in a pair of mirror nuclei. A more detailed description and investigation of Coulomb effects and studies of Mirror Energy Differences (MED) in mirror nuclei can be found in Ref. [3].

Together with significant theoretical effort the interpretation and understanding of Coulomb effects in mirror nuclei has increased substantially during recent years. However, almost all experimental studies of mirror nuclei have been limited to comparisons of excitation energies using MED values. This is mainly due to experimental difficulties of producing and detect the neutron deficient mirror partner with enough statistics to allow for more detailed spectroscopic measurements such as lifetimes of excited states. Such measurements in may provide useful information on, for example, effective transition operators when comparing the measured quantities with theoretical models. With improved experimental techniques these scenarios have started to become achievable during the last few years. Studies of spectroscopic quantities such as lifetimes of excited states and related electromagnetic properties of mirror nuclei can nowadays be looked upon. One example of investigating electromagnetic properties in mirror nuclei is the study of the $A = 51$ $T_z = \pm 1/2$ mirror pair, $^{51}_{26}\mathrm{Fe}_{25}$ and $^{51}_{25}\mathrm{Mn}_{26}$. In this study the lifetimes of the excited $27/2^-$ states are determined and used to probe the effective nucleon charges in the *fp*-shell. The data analysis in combination with theoretical simulations are described in detailed in section 4.3.1 and PAPER III. Bellow follows only a short description of the principle idea.

The level schemes of ^{51}Fe and ^{51}Mn are very similar as expected from the isospin formalism described above. Both nuclei can be described with their valence nucleons outside the $N = Z = 20$ shell closure distributed in the $1f_{7/2}$ orbitals. Within this re-

stricted configuration space there is only one possibility to align six (five) protons and five (six) neutrons for ^{51}Fe (^{51}Mn) to obtain the excited state with spin $27/2^-$. One other possibility to achieve this spin state would be to allow for particle excitations to the upper fp-shell ($2p_{3/2}$, $1f_{5/2}$, and $2p_{1/2}$ orbits). These excited $27/2^-$ states may mix with the the yrast $27/2^-$ state. However, large-scale shell-model calculations indicate that the mixing is small. The wave functions of the $27/2^-$ states can be used in simulations to calculate the reduced transition probabilities. By combining the theoretical simulations with the experimental values the effective nucleon charges are determined.

4.3 Data Analysis

Recorded raw data files are processed through various offline analysis packages before any physics analysis starts. This allows to perform redundancy checks, detector calibrations, data reformatting, and to sort data in various spectra and matrices for further processing. The number of packages employed strongly depends on the raw data structure and the physics aim. The most basic steps and their features in the process chain are:

- **Compression**: Removes unnecessary and incomplete data, i.e., data that do not contain all requested required signals or miss essential information.
- **Pre-sorting**: Perform alignment of time and energy signals for the various detectors utilized. This provides particle identification, from ancillary detector systems, and definition of prompt and delayed γ-ray transitions. The detectors are energy and efficiency calibrated and appropriate particle conditions are set before data is re-written to file.
- **Sorting**: Pre-sorted data is used to generate spectra and to create, for example, $\gamma\gamma$ matrices or $\gamma\gamma\gamma$ correlation cubes, which are used in the analysis.

A more detailed discussion on some of these steps can be found in, for example, Ref. [3, 17]. The final analysis is generally based on the output from the sorting phase, which allows to create and investigate spectra of various kinds. Further requirements can be introduced using different gate conditions on the data, thus generating specific spectra. For instance, $\gamma\gamma$ matrices and $\gamma\gamma\gamma$ cubes allow to perform coincidence spectroscopy, which can be used to select a specific nucleus, cascade, or transition.

4.3.1 Effective charges in ^{51}Mn and ^{51}Fe

An analysis of the $A = 51$ mirror nuclei has been performed based on data from the GASP03.12 experiment using the heavy-ion fusion-evaporation reaction ^{32}S $+^{24}$ Mg with a beam energy of 95 MeV. The ^{24}Mg target was mounted inside the Cologne plunger device in front of a stretched gold stopper foil and data were taken at target-stopper distances ranging from electric contact to 4.0 mm. The mirror nuclei ^{51}Fe and ^{51}Mn were produced via the evaporation of one α-particle and one neutron ($1\alpha1$n channel) and one α-particle and one proton ($1\alpha1$p channel), respectively. The $A = 51$ mirror pair has well established level schemes [32, 33, 34], which are shown in Fig. 4.4.

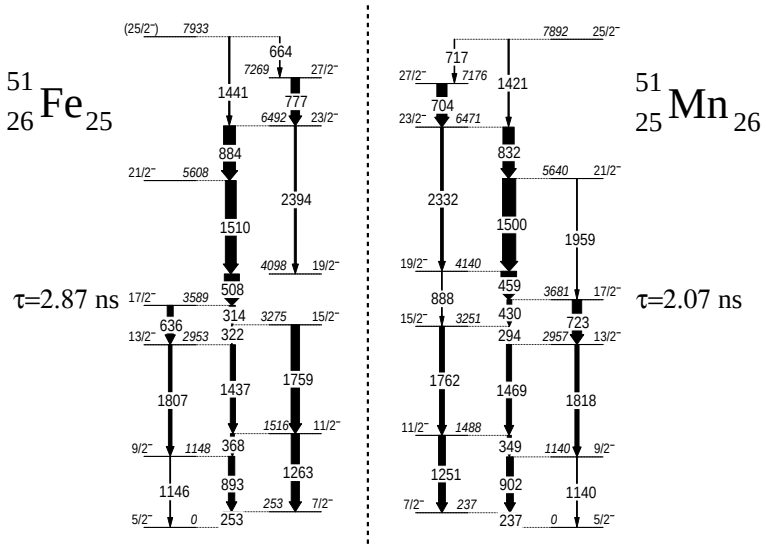

Figure 4.4: *Level schemes of the $A = 51$ mirror nuclei [32, 33, 34]. Energy labels are in keV and the widths of the arrows correspond to the relative intensities of the transitions.*

Data handling and experimental results

At first, the detectors are energy calibrated using ^{56}Co, ^{133}Ba, and ^{152}Eu standard calibration sources. Secondly, for each measured distance the time signals of the individual Ge detectors are aligned. During the same procedure detectors with corrupt or missing signals are masked out for further analysis. From the aligned Ge times the γ-ray transitions are assigned as being prompt or delayed by using a two-dimensional gate in a Ge-time vs Ge-energy matrix. With this gate condition set to assure that γ rays emitted from the $A = 51$ nuclei are within the gate, bad detectors excluded, and all calibrations done, the raw data was sorted. Data files acquired with the same conditions and at the same distances were added together. In total 21 files, corresponding to 21 distances, were created.

For each distance the events were sorted into $\gamma\gamma$ coincidence matrices with γ rays detected in one given detector ring placed along one axis and γ rays detected anywhere in the array along the second axis of the matrix. The γ rays were required to be detected in one of the seven detector rings and have an energy in the interval $0 < E_\gamma < 4096$ keV. Furthermore, to reduce the contribution from, for instance, Coulomb excitation in the gold stopper or random coincidences, a restriction on the total multiplicity of γ rays, M_γ, was used. The total multiplicity is the sum of the γ rays detected in the Ge-detectors and the BGO-elements. Only events with $M_\gamma > 6$ were used to create the $\gamma\gamma$ matrices. Spectra are obtained using the $\gamma\gamma$ matrices by an energy gate on one of the axis and projecting the coincidence spectrum on

the other axis. The width and placement of the energy gate can be determined by looking at the total projection, i.e., the projection of the full coincidence matrix on one axis. Figure 4.5 shows (a) the total projection and (b) a spectrum gated on the 237 keV transition in ^{51}Mn using all detector rings for data taken at a target-stopper distance of 1200 μm. Due to the relatively long distance Doppler shifted components can be observed for some of the transitions in the gated ^{51}Mn spectrum. The figure

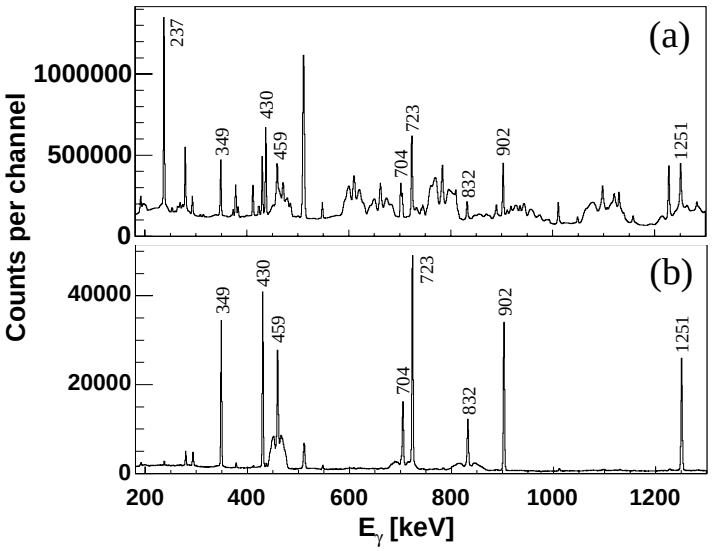

Figure 4.5: *(a) The total projection and (b) a spectrum in coincidence with the 237 keV transition in ^{51}Mn (b) for data taken at a target-stopper distance of* 1200 μm. *Energy labels of the peaks are in keV and correspond to transitions in ^{51}Mn.*

illustrates the effect of using γ rays in coincidence to obtain a clean spectrum, which later can be used in the analysis work. However, the quality of the resulting spectrum strongly depends on the gate conditions, i.e., how the peak and the background is selected. The exact setting of the energy gate might need to be reworked several times to optimize the result. This is done for all distances and detector rings and clean spectra gated on different transitions in ^{51}Mn and ^{51}Fe were collected.

Each target-stopper distance can be converted into a corresponding flight time using the velocity of the recoiling nucleus. The velocity can be derived from the shifted and unshifted Doppler components using

$$E_\gamma = E_0 \frac{\sqrt{1-\beta^2}}{1-\beta\cos\theta}, \tag{4.25}$$

where E_γ and E_0 are the measured energies of the two components, respectively, θ the angle to the detector with respect to the beam axis and β the recoil velocity in terms of the speed of light. Due to the symmetric geometry of the detector system the angle of the most forward, θ_f, and the most backward, θ_b, detector rings are situated

such that $\cos\theta_f = -\cos\theta_b = \cos\theta$. This allows to derive the recoil velocity using the two most outward detector rings as

$$\beta = \frac{\Delta E}{2E_0 \cos\theta}, \tag{4.26}$$

where a second order Taylor expansion of Eq. 4.25 has been used. ΔE is the energy difference between the shifted component measured in the forward and backward detector ring and E_0 the measured energy of the unshifted component.

The recoil velocity was determined using the intense 1500 keV $21/2^- \rightarrow 19/2^-$ transition obtained in coincidence with the 237 keV ground-state transition in ^{51}Mn. The velocities range from 3.7% to 4.1% of the speed of light for the three different targets used during the experiment. The variation in velocity can be explained by the fact that the three targets had slightly different thicknesses, which will give rise to somewhat different velocities. The respective individual recoil velocity for each target-distance combination is later used in the analysis for the conversion of the target-stopper distance to flight time.

The method used to determine the lifetimes of the $27/2^-$ states in the $A = 51$ mirror pair is based on very specific features of their decay schemes. They consist of essentially three regimes: the transitions below the isomeric $17/2^-$ states, those feeding into the long-lived ($\sim$ 100 ps) $27/2^-$ states, and the short-lived states in between (see Fig. 4.4). Due to the isomeric $17/2^-$ states low-lying transitions are essentially always emitted from stopped residues independently of the target-stopper distance used. Thus for spectra taken in coincidence with these low-lying transitions it is possible to apply the RDDS method to the transitions between the $27/2^-$ and the $17/2^-$ states. To avoid that Doppler shifted and unshifted components interfere only the two most forward and two most backward detector rings are used, for which the two components of the coincident transitions are well separated. This interference effect is mostly observed for the larger target-stopper distances, because more and more γ-rays are emitted in-flight than as stopped. Figure 4.6 illustrates how the target-stopper distance affects the intensities of the stopped and Doppler shifted components. The spectra are obtained by gating on the low-energy 253 keV $7/2^- \rightarrow 5/2^-$ transition in ^{51}Fe for distances of 400 μm (Fig. 4.6a) and 1200 μm (Fig. 4.6b). For the short distance (400 μm) the four transitions at 636, 777, 884, and 893 keV in ^{51}Fe are clearly seen as stopped peaks. When increasing the distance to 2000 μm the stopped components of the two transitions at 777 and 884 keV are significantly reduced and Doppler shifted 'wings' arise on each side of the stopped peaks. The 636 and 893 keV transitions are still observed as stopped peaks, because they are situated below the isomeric $17/2^-$ state and the flight distance is still rather short with respect to its lifetime.

The lifetime analysis for the $27/2^-$ states in the $A = 51$ mirror pair employ the same analysis method for both nuclei. This method was developed using data only originating from the ^{51}Mn nucleus due to the large amount of statistics compared to the very weakly populated mirror nucleus ^{51}Fe. The large amount of statistics in the ^{51}Mn case also allows for a detailed investigation of possible systematic errors and to achieve proper normalization coefficients for each distance. The latter are required for a normalization of the measuring times and beam currents between the different distances. Several methods were investigated in detail to obtain a good set of normalization coefficients. Some of these methods were:

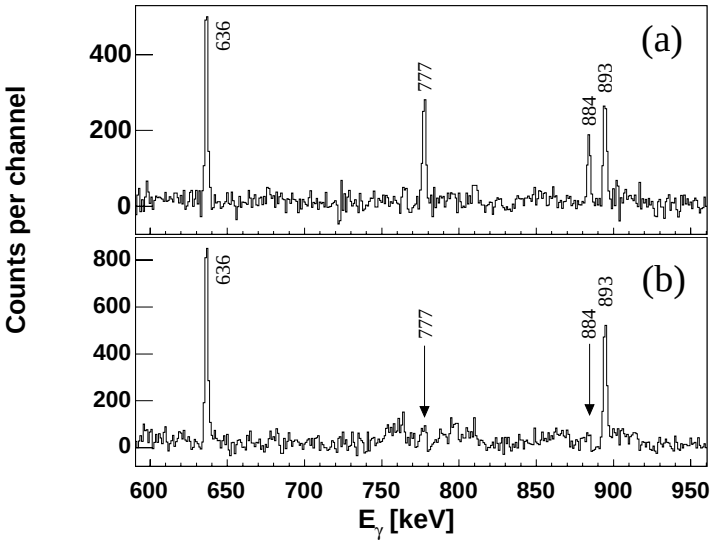

Figure 4.6: *Spectra taken in coincidence with the* $7/2^- \rightarrow 5/2^-$ *253 keV transition in* ^{51}*Fe for the two most forward and two most backward detector rings of GASP. Panel (a) shows spectra obtained with target-stopper distance* 400 μm *and panel (b) for the distance* 1200 μm. *Energy labels of the peaks are in keV.*

- The intensity of the unshifted 237 keV transition in ^{51}Mn and correct the value for the decay from the known lifetime of the $17/2^-$ state.
- The intensities of the shifted and unshifted components of the transition itself.
- The intensities of the shifted and unshifted components for the 832 keV transition taken in coincidence with the 237 keV transition in ^{51}Mn.
- The intensities of the shifted and unshifted components for the 459 keV transition taken in coincidence with the 237 keV transition in ^{51}Mn.
- Only detectors situated at 90° with respect to the beam axis.
- Transitions from other nuclei, for example, ^{53}Fe.
- The number of counts in the total projection.

Because of, for example, difficulties with background subtraction, the influence in spectra from β-decaying nuclei, the limited amount of statistics for selected transitions, etc. the investigated methods were more or less applicable. It was found that the most appropriate normalization coefficients were obtained using the 459 or 832 keV transitions. Hence, further analysis employ the coefficients obtained using the combined intensities of the shifted and unshifted Doppler components for both the 459 and 832 keV transitions. The intensities for these transitions observed in

all detector rings were summed up in spectra taken in coincidence with the 237 keV ground-state transition in ^{51}Mn and then used as normalization coefficients. As the relative statistics of ^{51}Mn and ^{51}Fe in the collected data are expected to be the same for different distances the same normalization coefficients can be used for both nuclei.

Due to the special features of the $A = 51$ decay schemes the lifetime of the $27/2^-$ states in the mirror pair can in principle be extracted analysing any of the transitions located between the $27/2^-$ and $17/2^-$ states. Nevertheless, to eliminate contributions from possible side feeding an analysis of the 704 keV and the 777 keV $27/2^- \rightarrow 23/2^-$ transitions for ^{51}Mn and ^{51}Fe, respectively, is preferred. To perform an analysis of the very weakly populated ^{51}Fe nucleus the measured distances needed to be combined into nine effective distances: 6.5(1), 17.7(1), 42.7(7), 125(3), 404(11), 701(16), 1198(29), 1984(60), and 4000(100) μm. This merge was done using the extracted normalization coefficients as weighting factors and the effect on the result using nine distances compared to all 21 distances was investigated using the ^{51}Mn sample, for which each individual distance can be used in the analysis.

For ^{51}Mn it was found that an analysis of the 704 keV transition was hampered due to Doppler shifted components of the 723 keV $17/2^- \rightarrow 13/2^-$ and 717 keV $25/2^- \rightarrow 27/2^-$ transitions as well as background radiation at 701 keV from the decay of the $19/2^-$ isomer in ^{53}Fe. Instead the analysis was performed using the 459 and 832 keV transitions in spectra obtained in coincidence with the 237 keV ground-state transition. To account for the side feeding their decay curves were fitted with a short ($\tau < 10$ ps) and a long lifetime component. The analysis of the two transitions was carried out in parallel for each measured distance and individual detector rings. The results were found to be consistent with each other. The final result was obtained as the weighted mean of the results from the individual detector rings using only the 832 keV transition as the amount of side feeding is expected to be less for this transition compared to the 459 keV transition.

The analysis of ^{51}Fe was performed using the 777 keV transition for nine effective distances where the data points were fitted with an exponential to extract the lifetime. To increase the statistics, spectra in coincidence with the 253, 314, and 636 keV transitions from the two most forward and the two most backward detector rings were summed. Since a stopped component of the 777 keV line was absent in the spectrum taken at the largest distance it was excluded from the analysis. Figure 4.7 illustrates the decay curves of the 777 keV $27/2^- \rightarrow 23/2^-$ transition in ^{51}Fe and the $23/2^- \rightarrow 21/2^-$ 832 keV transition in ^{51}Mn.

The resulting lifetimes of the $27/2^-$ states in ^{51}Mn and ^{51}Fe with the corresponding $B(E2; 27/2^- \rightarrow 23/2^-)$ values are listed in Table 4.1. The $B(E2)$ values are derived from Eq. 4.12 using the extracted lifetimes and $E_\gamma = 704.4(5)$ keV and $E_\gamma = 777.1(5)$ keV for ^{51}Mn and ^{51}Fe, respectively. The ratio, R, between the $B(E2)$ values of the mirror transitions in ^{51}Fe and ^{51}Mn is $R = 0.884(22)$. The error ratio is merely statistical. The systematic uncertainty in the lifetimes is related to the normalization and the exact determination of the yield of the stopped component at large distances. Other contributions are the possible short-lived ($\tau < 1$ ps, cf. [34]) feeding into the $27/2^-$ state, and combining the results from individual detector rings and the 21 single distances used in the measurement into nine effective distances, which is necessary for the analysis of the very weakly populated mirror nucleus ^{51}Fe.

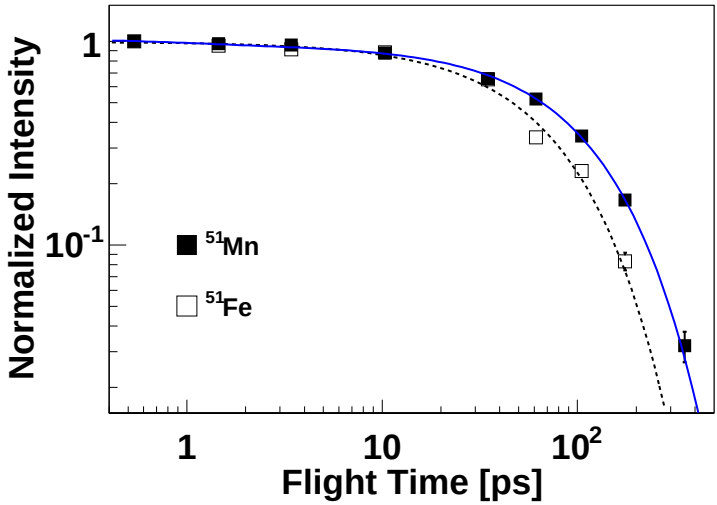

Figure 4.7: *Decay curves for the 832 keV transition in ^{51}Mn (solid) and the 777 keV transition in ^{51}Fe (dashed) for nine effective flight distances.*

Table 4.1: *Values for the extracted lifetimes and the corresponding $B(E2)$ values for the $27/2^-$ states in the mirror nuclei ^{51}Mn and ^{51}Fe.*

	Lifetime [ps]	$B(E2)$ [e^2fm^4]	$B(E2)$ [W.u.]
^{51}Mn	$100.7 \pm 1.2 \pm 3$	46.7(14)	4.16(12)
^{51}Fe	$69.7 \pm 1.6 \pm 3$	41.3(24)	3.68(21)

Calculations performed to determine the effective charges

To study the consequences of the lifetime results on polarization charges large-scale shell-model calculations were performed using the shell-model code ANTOINE [30, 31]. The calculations employ the full fp space containing the $1f_{7/2}$ orbit below and the $2p_{3/2}$, $1f_{5/2}$, and $2p_{1/2}$ orbits above the $N = Z = 28$ shell closure. The configuration space was truncated to only allow for excitations of up to five particles across the shell closure. This configuration space provides predictions more or less indistinguishable from calculations using the full fp space [35]. Three interactions have been studied in detail: The standard KB3G [35] interaction without any Coulomb interaction, the KB3G interaction with theoretical harmonic-oscillator Coulomb matrix elements (Coulomb HO), and the KB3G interaction with the $1f_{7/2}$ Coulomb matrix elements replaced with the experimental values from the $A = 42$ mirror pair (Coulomb A42).

The investigation of the effective charges utilizes three input parameters to the simulations; the isoscalar and isovector polarization charges, $e_{pol}^{(0)}$ and $e_{pol}^{(1)}$, and the harmonic oscillator parameter, b_0 (cf. section 4.1). As the simulations aim to repro-

duce the two experimental $B(E2)$-values and their ratio simultaneously the study is carried out utilizing an iterative process for different combinations of the three parameters. The method to determine the effective charges using the Coulomb A42 interaction is described in detail in the following. The same method is employed for calculations using the other interactions.

Assuming identical orbital radii, i.e., the same b_0 for ^{51}Mn and ^{51}Fe the $B(E2)$-values for the $27/2^- \rightarrow 23/2^-$ mirror transitions were calculated. The harmonic oscillator parameter was set to $b_0 = 1.01$ in all calculations while the polarization charges were varied over different intervals. For a given isoscalar value calculations were performed with the isovector parameter varied in the region $0.0 < e^{(1)}_{pol} < 1.0$. For each calculation the ratio, R, between the resulting $B(E2)_{\rm Fe}$ and $B(E2)_{\rm Mn}$ values is determined and plotted versus the isovector parameter. The values are fitted to a third degree polynomial and compared to the $B(E2)$-ratio derived from the experimental results, $R_{exp} = 0.884(22)$. Fig. 4.8 illustrates the isovector polarization charge as a function of the $B(E2)$-ratio from the shell-model calculations, when the isoscalar polarization charge is set to $e^{(0)}_{pol} = 0.5$.

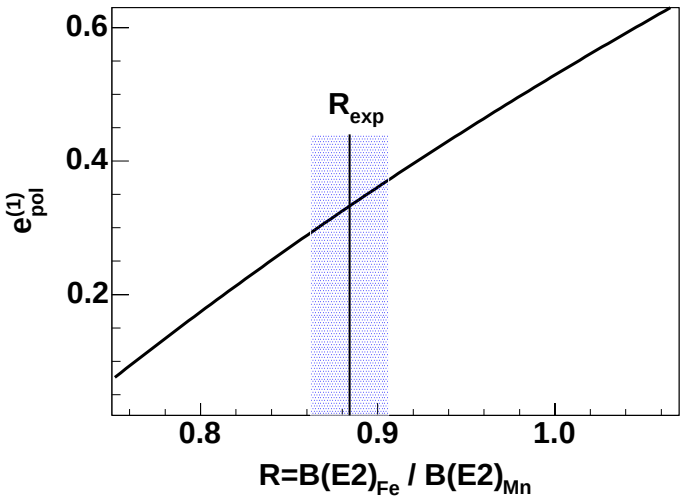

Figure 4.8: *The isovector component as function of the $B(E2)$-ratio from shell-model calculations using the Coulomb A42 interaction with $b_0 = 1.01$ and $e^{(0)}_{pol} = 0.5$. The experimental ratio is illustrated with the vertical line at $R_{exp} = 0.884(22)$.*

Thus, the isovector component can be derived for a given isoscalar component. These polarization charges experimental $B(E2)$-ratio but not necessary the absolute $B(E2)$-values for ^{51}Fe and ^{51}Mn. To find a solution that simultaneously reproduces the absolute $B(E2)$-values and their ratio the harmonic oscillator parameter is ad-

justed according to (cf. Eq. 4.16 and Eq. 4.17)

$$b_0 = 1.01 \left(\frac{B(E2)_{exp}}{B(E2)_{the}} \right)^{1/4}. \tag{4.27}$$

A change of b_0 will affect the absolute $B(E2)$-values, but keep their ratio as the orbital radii are assumed to be identical for the two members of the mirror system. Thus a simulation performed with the adjusted b_0 parameter and the corresponding polarization charges will reproduce the experimental $B(E2)$-values and their ratio simultaneously. Table 4.2 lists values of the isoscalar and isovector polarization charges with the resulting $B(E2)$-values using $b_0 = 1.01$. These values do not reproduce the experimental values but can be used to determine the adjustment of b_0 according to Eq. 4.27. The corresponding b_0 values required to reproduce the absolute values are also listed in Table 4.2.

Table 4.2: *Polarization charges employed in shell-model calculations with the resulting $B(E2)$-values for calculations performed with the Coulomb A42 interaction and harmonic oscillator parameter $b_0 = 1.01$. A change to the b_0 values in the last row of the table are required to reproduce the experimental $B(E2)$-values (cf. Table 4.1).*

$e_{pol}^{(0)}$	0.300	0.400	0.500	0.600	0.700
$e_{pol}^{(1)}$	0.365	0.348	0.331	0.314	0.297
$B(E2)_{Fe}$	27.93	35.35	43.64	52.80	62.83
$B(E2)_{Mn}$	31.63	40.03	49.42	59.80	71.17
b_0	1.113	1.049	0.995	0.949	0.909

Based on the adjusted b_0 parameter and the corresponding polarization charges a dependence between the three parameters is derived for which the individual $B(E2)$ values are reproduced. The isoscalar and isovector polarization charges are plotted versus the harmonic oscillator parameter and fitted by second degree polynomials. Figure 4.9 illustrates this dependence for the Coulomb A42 interaction. From this dependence a combination of the three parameters is determined for each b_0-value that, when employed in the shell-model calculations, would reproduce the experimental values and their ratio simultaneously.

As discussed in previous sections the harmonic oscillator parameter is commonly set to $b_0 = 1.01$ (cf. Eq. 4.17), which leads to an isoscalar and isovector polarization charge of $e_{pol}^{(0)} = 0.47$ and $e_{pol}^{(1)} = 0.34$ using the Coulomb A42 interaction. Using Eq. 4.20 the corresponding effective charges are 1.13 and 0.81 for the proton and neutron, respectively.

The dependence between the three parameters was derived for the other interactions as well. Figure 4.10 illustrates this dependence for two different sets of Coulomb matrix elements and one set without any Coulomb interaction. In all three cases the nuclear interactions are based on the KB3G interaction. From Fig. 4.10 it is seen that the isoscalar component is more sensitive to changes in b_0, i.e., the nuclear radii, than the isovector component. This is because the effective proton and neutron

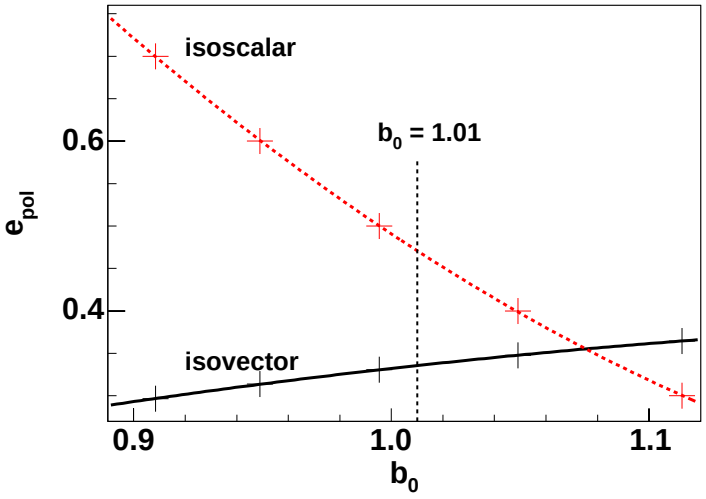

Figure 4.9: *Dependence of the three parameters b_0 and the isoscalar and isovector polarization charges for the Coulomb A42 interaction. A given combination of the three parameters reproduces the experimental $B(E2; 27/2^- \rightarrow 23/2^-)$ values in the $A = 51$ mirror nuclei and their ratio.*

charges are affected by the isoscalar part equally while the isovector part affects the effective charges with opposite sign. On the other hand, the isoscalar part is rather independent of the choice of $1f_{7/2}$ Coulomb matrix elements, whereas the isovector part shows a stronger dependence.

Table 4.3 lists the extracted isoscalar and isovector polarization charges for three different KB3G interactions using the harmonic oscillator parameter $b_0 = 1.01$. For comparison a calculation with the FPD6 [36] interaction is included. Using the experi-

Table 4.3: *Isoscalar and isovector polarization charges, which simultaneously reproduce the $B(E2; 27/2^- \rightarrow 23/2^-)$ values in the $A = 51$ mirror nuclei, for different shell-model calculations using $b_0 = 1.01$*

	no Coulomb	Coulomb HO	Coulomb A42	FPD6
$e_{pol}^{(0)}$	0.466(3)	0.466(3)	0.471(2)	0.632
$e_{pol}^{(1)}$	0.316(26)	0.310(37)	0.336(37)	0.315

mental $B(E2)$-values and their errors, the uncertainties in $e_{pol}^{(0)}$ and $e_{pol}^{(1)}$ are determined by reproducing the maximum (minimum) $B(E2; 27/2^- \rightarrow 23/2^-)$ value in ^{51}Mn and minimum (maximum) $B(E2; 27/2^- \rightarrow 23/2^-)$ value in ^{51}Fe, respectively. Due to the time-consuming calculations no uncertainty for the extracted polarization charges was

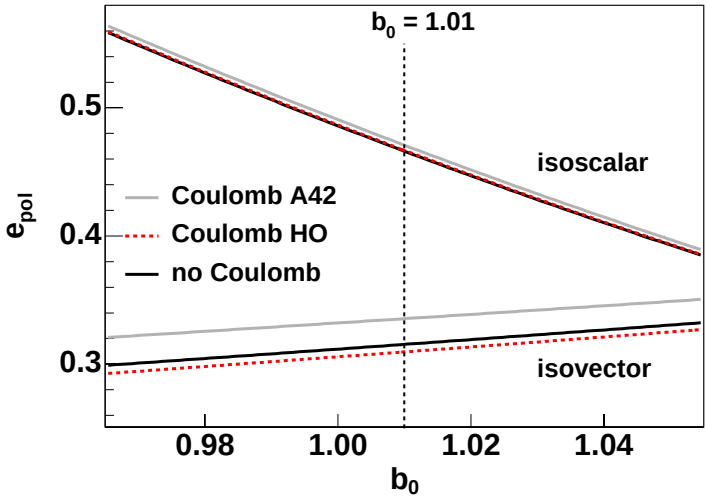

Figure 4.10: *Polarization charges, necessary to reproduce the* $B(E2; 27/2^- \rightarrow 23/2^-)$ *values in the* $A = 51$ *mirror nuclei, as a function of* b_0 *for three different shell-model calculations.*

estimated for FPD6, but it is expected to be in the same order of magnitude as the calculations performed with the KB3G interaction.

The results in Table 4.3 are in very good agreement with Eq. 4.21, which for $N = Z$ nuclei gives $e_{pol}^{(0)} = 0.5$ and $e_{pol}^{(1)} = 0.32$. The corresponding effective charges obtained using Eq. 4.20 gives $\varepsilon_p \sim 1.15\ e$ and $\varepsilon_n \sim 0.80\ e$ for the proton and neutron, respectively. As mentioned above, an increase of the nuclear radii for the two mirror nuclei will result in smaller effective charges to preserve the reduced $E2$-transition probabilities.

Depending on the interaction used in the shell-model calculations somewhat different results are obtained (cf. Table 4.3). However, an observation is that calculations performed with Coulomb interaction (Coulomb HO and Coulomb A42) results in polarization charges smaller and larger than the results from the calculation without any Coulomb interaction. This phenomenon is seen in the isovector polarization charge in Fig 4.10. An investigation, utilizing several shell-model calculations, has been performed to try and understand the origin of this effect. The two different sets of Coulomb matrix elements are listed in Table 4.4.

Table 4.4: *Values of the* $1f_{7/2}$ *Coulomb matrix elements in MeV used in shell-model calculations for two different interactions.*

	$J = 0$	$J = 2$	$J = 4$	$J = 6$
Coulomb HO	-1.527	-0.666	0.127	0.426
Coulomb A42	-1.527	-0.754	0.115	0.479

The calculations were carried out using the same iteration method as described above. A "dummy" interaction was customized by manipulating the Coulomb A42 interaction such that only one of the four Coulomb matrix elements listed in Table 4.4 differed from the Coulomb HO interaction. In this way the effect of each individual Coulomb matrix element can be studied. It was found that mainly the $J = 6$ matrix element is responsible for the above mentioned phenomenon.

The polarization charges above are extracted under the assumption that the orbital radii of the two mirror nuclei are identical (b_0 is the same for both members). However, it is reasonable to assume that the Coulomb interaction pushes the proton wave functions towards larger radii with respect to the neutron wave functions. Thus, the radius of ^{51}Fe could be slightly larger than the radius of ^{51}Mn, while on the other hand shell-model calculations indicate that mostly neutrons (protons) are active in the $B(E2)$ transitions in ^{51}Fe (^{51}Mn). A detailed investigation of the effective charges taking radial effects into account is certainly interesting but requires more experimental data to account for the extra degree of freedom.

A simple study of the polarization charges assuming different radii for the two mirror nuclei has been performed. The harmonic oscillator parameter was fixed to $b_0 = 1.01$ for ^{51}Mn while it was varied in the interval $0.99 < b_0 < 1.03$ for ^{51}Fe. The derivation of the isovector and isoscalar components employed the same method as described previously. Due to the time consuming shell-model calculations this investigation was performed only with the Coulomb A42 interaction. Figure 4.11 illustrates the dependence of the two polarization charges when changing b_0 for ^{51}Fe while keeping the value for ^{51}Mn fixed at $b_0 = 1.01$. The figure isovector component

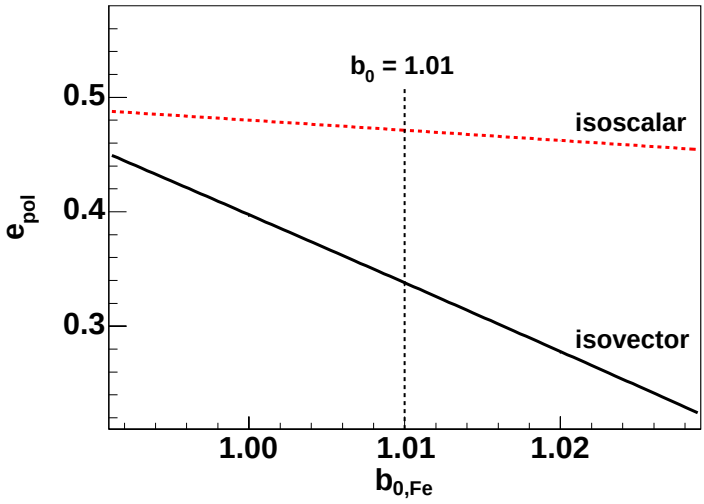

Figure 4.11: *Polarization charges necessary to reproduce the* $B(E2; 27/2^- \rightarrow 23/2^-)$ *values in the* $A = 51$ *mirror nuclei, using a fixed radius for* ^{51}*Mn* ($b_0 = 1.01$) *and varying the radius for* ^{51}*Fe,* $b_{0,\mathrm{Fe}}$*. The results are based on shell-model calculations using the Coulomb A42 interaction.*

is more sensitive than the isoscalar component. This is the opposite as compared to the situation illustrated in Fig. 4.10 where the nuclear radius of both mirror nuclei was changed simultaneously. In the present scenario, however, the isovector part can compensate for different nuclear radii as it affects the effective proton and neutron charges with opposite signs.

4.3.2 Excited states in ^{53}Fe

A detailed analysis of excited states in $^{53}_{26}Fe_{27}$ has been performed using data from three experiments: the GSFMA73 experiment, the GS2k017 experiment, and the GASP03.12 experiment. From the obtained results, a largely extended level scheme was constructed and the lifetime of a few of the newly observed excited states were measured. Part of the ^{53}Fe level scheme is illustrated in Fig. 4.12. The full extended level scheme can be found in PAPER V.

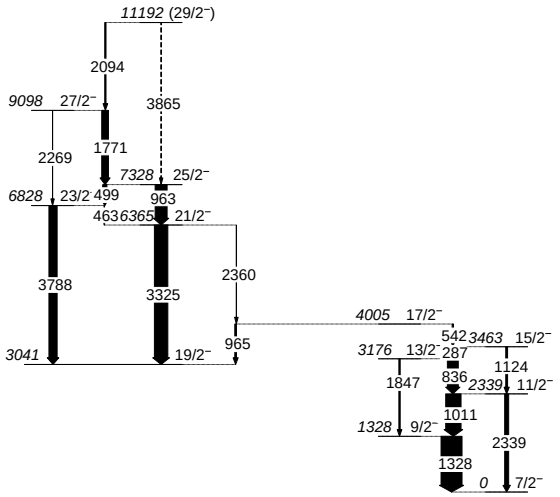

Figure 4.12: *Relevant part of the level scheme of ^{53}Fe. Energy labels are in keV and the widths of the arrows correspond to the relative intensities of the transitions.*

Data handling and experimental results

The details of the data handling and the analysis of the two Gammasphere experiments have been described earlier in, for example, Ref. [3, 17, 37]. A summary of the analysis and the experimental results in form of the extended level scheme is found in PAPER V. The basic data handling of the GASP03.12 experiment was performed as described in section 4.3.1. The sorting of events into $\gamma\gamma$ coincidence matrices, the determination of the intensities of the relevant shifted and unshifted 963 keV and 3325 keV transitions (cf. Fig. 4.12), and the merge into 14 effective flight times used in the analysis are described in PAPER V.

The lifetimes of the first excited $21/2^-$ and $25/2^-$ states in ^{53}Fe were determined using standard RDDS technique (cf 2.1.2). Hence, using the stopped components for the 963 keV $25/2^- \rightarrow 21/2^-$ and the 3325 keV $21/2^- \rightarrow 19/2^-$ transitions, the result is $\tau = 26.2(32)$ ps and $\tau < 4$ ps for the $25/2^-$ state and the $21/2^-$ state, respectively. A more detailed description of the RDDS analysis can be found in PAPER V. Note the difference between the $A = 51$ and $A = 53$ analyses, which both utilize the RDDS technique but for spectra obtained in coincidence with transitions below and above the state of interest, respectively.

Shell-Model Interpretation

The excited states in ^{53}Fe were compared to large-scale shell-model calculations that employ the full fp shell and were performed using the shell-model ANTOINE (cf. section 4.3.1). At first, the influence on the result due to the number of allowed particle exciations, t, from the $1f_{7/2}$ shell to the upper fp shell was investigated. Figure 4.13 shows the resulting energy levels from calculations using the KB3G interaction with theoretical harmonic-oscillator Coulomb matrix elements for $t = 0,\ 1,\ ...,\ 5$. Allowing

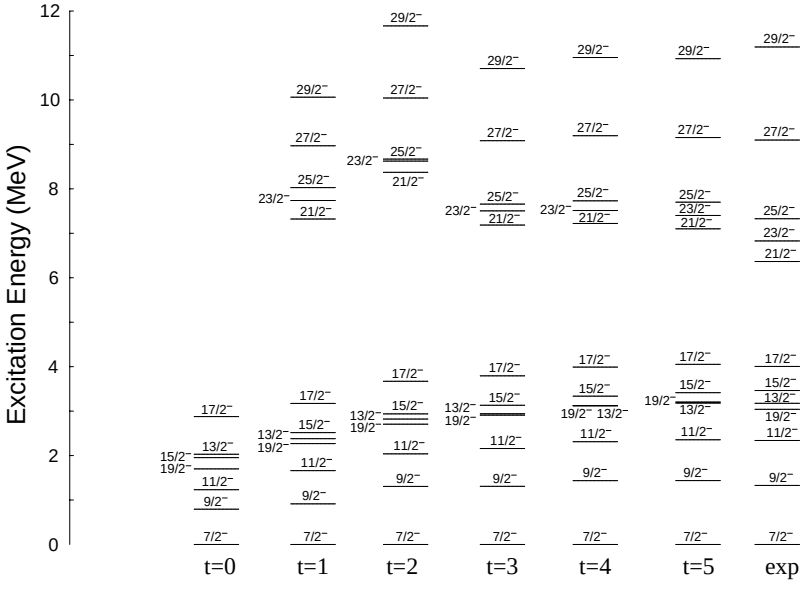

Figure 4.13: *Calculated energy levels of ^{53}Fe allowing for t nucleons to be excited from the $1f_{7/2}$ shell to the upper fp shell. The experimental energy levels are included for comparison.*

for only a few particle excitations it is clear that the calculated level scheme is suppressed with respect to the experimental level scheme. However, with increasing number of particle excitations the calculated energy levels converge towards the observed

energies and the experimental level sequence is better reproduced.

Further calculations were performed using four different interactions. The calculated level energies and their electromagnetic properties are compared to the experimental results. Also an investigation on effective g-factors, using effective charges as derived in section 4.3.1, was performed. A more detailed description of the calculations and the results can be found in PAPER V.

4.3.3 Excited states in ^{54}Ni

Based on the known level scheme of $^{54}_{26}Fe_{28}$ [38, 39] one expects to observe a long-lived 10^+ state followed by a five-step γ-ray cascade in the mirror nucleus $^{54}_{28}Ni_{26}$. Figure 4.14a illustrates the relevant part of the ^{54}Fe level scheme with the isomeric 10^+ state. The state has a lifetime of $\tau = 525(10)$ ns and decays via the 146 keV $E2-$ and the 3578 keV $E4-$transitions. Simple shell-model calculations utilizing the full fp shell, but limited to allow for only two particle excitations across the $N = Z = 28$ shell closure, have been performed to estimate the lifetime of the corresponding 10^+ state in ^{54}Ni. The calculations for ^{54}Ni include same $E4$ strenghts as experimentally known in ^{54}Fe. From the resulting $B(E2)$ values the lifetime of the 10^+ state is calculated as function of the $E2$ transition energy using Eq. 4.12. Figure 4.14b shows the estimated lifetime of the 10^+ state in ^{54}Ni as function of the $10^+ \rightarrow 8^+$ $E2$ transition energy.

Hence, measurements of the $10^+ \rightarrow 8^+$ $E2$ and the $10^+ \rightarrow 6^+$ $E4$ transitions in ^{54}Ni will serve as a consistency check of the nuclear shell model. In particular, a comparison with experimental data for ^{54}Fe allows for a similar study on effective charges as discussed in section 4.3.1, which may provide additional information on this phenomenon. The effective charges for the $A = 54$ mirror pair can be determined using the known liftetime and the branching ratio of the 10^+ isomer in ^{54}Fe and the corresponding, so far unknown, properties of the mirror state in ^{54}Ni. Furthermore, it is also of interest to study the Mirror Energy Differences for the $A = 54$ nuclei and compare them to the $A = 42$ nuclei ($^{42}_{22}Ti_{20}$ and $^{42}_{20}Ca_{22}$). The present analysis aims to identify and determine the level scheme structure for ^{54}Ni with focus at and around the expected isomeric 10^+ state. Lower lying excited states (2^+, 4^+, 6^+) have been observed in an Euroball experiment but are not yet published [40].

The present analysis is based on combined data from the GSFMA73 and GS2k017 experiments (cf. section 2.2). The ^{54}Ni nuclei are populated through the very weak $1\alpha 2n$ reaction channel. Hence, the analysis requires the detection of two correlated neutrons. In order to obtain reasonably high statistics but still a clean $1\alpha 2n$-spectrum, extremely good and efficient neutron discrimination is needed. Problems with false two-neutron events, which arise due to neutron scattering, also need to be taken into consideration as they contaminate the $2n$-gated spectra. Neuterons are distinguished between γ rays using different gate conditions, which allow to defines whether a neutron or a γ ray hit a specific detector module. The neutron gate conditions have been reworked several times to optimize the result for the present analysis. A more detailed desription of the particle identification and the different spectra used in the neutron discrimination process can be found in Ref. [41]. Due to the relatively low two-neuteron detection efficiency one can expect to observe ^{54}Ni also in the $1\alpha 1n$-gated spectra. Therefore, both the $1\alpha 1n$- and the $1\alpha 2n$-gated data sets are used in the analysis and sorted into $\gamma\gamma$-matrices.

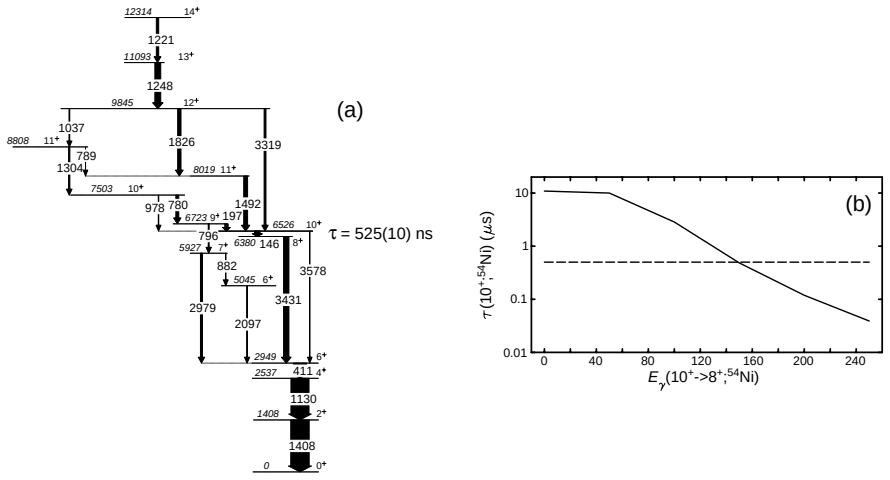

Figure 4.14: *(a) Relevant part of the level scheme of* ^{54}Fe*. The lifetime of the* 10^+ *state is indicated. Energy labels are in keV and the widths of the arrows correspond the relative intensities of the transitions. (b) The lifetime of the corresponding* 10^+ *state in* ^{54}Ni *as function of the* $10^+ \rightarrow 8^+$ $E2$ *transition energy.*

In order to fine tune the analysis the detected γ rays are assigned as being prompt, delayed, or isomeric. This allows to split up the constructed matrices into prompt, delayed, and isomeric parts, respectively. Isomeric γ rays are emitted once the residual nuclei are stopped whereas prompt and delayed γ rays arise from transitions when the nuclei are still in flight. To distinguish between prompt and delayed γ rays, the latter are defined using time gates next to the prompt time peak. The present reaction is believed to populate ^{54}Ni jsut above the proposed isomeric 10^+ state. Lower lying transitions are most likely to be found among the isomeric γ rays, whereas transitions above the 10^+ state shall be found as prompt γ rays. It can be concluded, with available statistics, that no transition corresponding to ^{54}Ni is seen in spectra comprising delayed or isomeric γ-rays. This indicates that the lifetime of the 10^+ state is longer than the corresponding state in ^{54}Fe, as the known γ-ray energies for the $6^+ \rightarrow 4^+ \rightarrow 2^+ \rightarrow 0^+$ cascade [40] are not at all observed. Hence, the continued analysis focuses on data with prompt γ-rays.

The prompt spectrum showed a promising peak at around 191 keV, which may correspond to the 197 keV $9^+ \rightarrow 10^+$ transition in ^{54}Fe. From the proposed similarities with the ^{54}Fe level scheme (cf. Fig. 4.14), one then also expects to see one peak around 780 keV and one peak around 1305 keV in coincidence with this 191 keV transition. In a spectrum obtained in coincidence with the 191 keV transition, four

peaks at 752, 1032, 1061, and 1098 keV are observed. It can, however, be concluded that these four peaks arise from ^{65}Ga [42]. The prompt 1α2n-gated spectrum and the spectrum obtained in coincidence with the 191 keV transition is shown in Fig. 4.15. The spectra clearly show the peaks from ^{65}Ga. There is also a tiny fraction of ^{51}Mn leaking through.

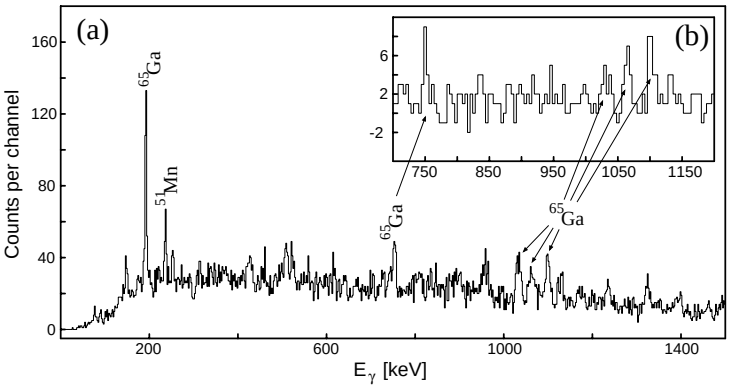

Figure 4.15: *(a) The total projection of the prompt* 1α2n*-gated spectrum. (b) The spectrum in coincidence with the 191 keV line is inserted at the top. The lines from* ^{65}*Ga nuclei at 752, 1032, 1061 and 1098 keV are clearly seen in the coincidence spectrum.*

The peaks corresponding to ^{65}Ga arise from a contamination in the ^{28}Si targets. To prevent them to oxidize, they were placed in a sealed container comprising argon atmosphere. However, instead of contamination from oxidation in air, ^{40}Ar atoms diffused into the target. Thus fusion-evaporation reactions with the ^{32}S beam on ^{40}Ar are possible, producing ^{72}Se as the compound nucleus. The ^{65}Ga nuclei are populated in the 1α2n1p-channel, but because of the finite proton and neutron detection efficiency it is also seen in the 1α1n- and 1α2n-spectra.

To reduce the amount of ^{65}Ga in the 1α2n-specta a restriction on the total number of γ rays, M_γ, is introduced. M_γ is the sum of γ-rays detected in the Ge-detectors and in the BGO-elements. Through comparison of two 1α2n-gated spectra with $M_\gamma \leq 5$ and $M_\gamma \geq 7$, respectively, it is found that the amount of ^{65}Ga is significantly higher in the latter case. Hence, to remove the contamination of ^{65}Ga, the two spectra were normalized to the strong 191 keV transition in ^{65}Ga and the spectrum obtained with $M_\gamma \geq 7$ was subtracted from the spectrum obtained with $M_\gamma \leq 5$. The resulting spectrum is found to be much cleaner. This spectrum is believed to reflect the primary reaction, in which peaks from the ^{54}Ni nuclei are expected to be present. By studying this spectrum, which is shown in Fig. 4.16, peaks at 1040 keV and 1327 keV can be observed. They belong to the ^{32}S+^{28}Si reaction, but unfortunatley not to ^{54}Ni. They are known transitions in ^{53}Co [43], which is the 1α2n1p reaction channel.

It is concluded that no peaks arising from the ^{54}Ni nuclei can be observed with good accuracy in any of the, so far, produced spectra. It is believed that due to the

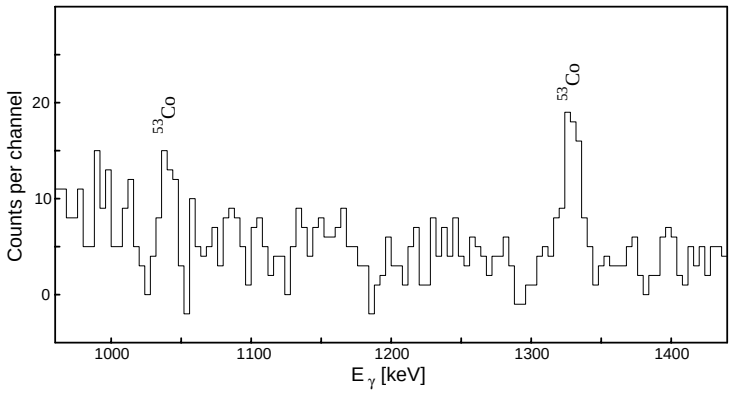

Figure 4.16: *The resulting spectrum obtained by subtracting two spectra as described in text. The reduced amount of* ^{65}Ga *and the two peaks at 1040 and 1327 keV, correspondig to known transitions in* ^{53}Co*, are clearly seen.*

long lifetime of the proposed 10^+ state one would not get enough γ-rays from either above or below the isomer, to fire the event trigger.

Chapter 5

Conclusion and Outlook

The first part of the present thesis discusses the first measurements of deuterons and anti-deuterons produced in $\sqrt{s_{NN}} = 200$ GeV gold-gold collisions at RHIC, performed within the PHENIX experiment. Invariant yields and transverse momentum spectra are presented. In combination with measured (anti-)proton spectra the coalescence parameter, B_2, was investigated. The increase of B_2 with transverse momentum is inconsistent with a simple model and indicates a decreasing source size with increasing momentum, which is indicative of an expanding source.

Future analysis work would, of course, be to analyse data with higher statistics to improve the results for the (anti-)deuterons and also allow for a search and measurements of heavier anti-nuclei, for example, anti-triton or anti-helium. However, an analysis of (anti-)deuterons in data from proton-proton collisions, where no collective transverse flow is expected, may also provide valuable information. The results obtained in such measurements should yield a smaller source size compared to that obtained from gold-gold collisions.

The second part of the thesis discusses lifetime measurements of excited states of atomic nuclei and illustrates how such measurements are utilized to access and determine effective transition operators. In particular, the lifetime of the analogue $27/2^-$ states in the $A = 51$ mirror pair have been measured. This allow to determine the corresponding $B(E2; 27/2^- \rightarrow 23/2^-)$ values, which are employed in an unique investigation of the effective nucleon charges near the doubly magic nucleus ^{56}Ni. A detailed comparison with large-scale shell-model calculations yields the effective charges of $\varepsilon_n \sim 0.80$ and $\varepsilon_p \sim 1.15$ for the neutron and proton, respectively. A more extensive study on the phenomenon of effective charges requires additional experimental data on nuclei in the fp shell. A similar study may be performed in the $A = 54$ mirror pair with the long-lived 10^+ state in ^{54}Fe and the corresponding, so far unknown, analogue state in ^{54}Ni.

An analysis based on data from two different experiments aiming at identification of γ-ray transitions in the ^{54}Ni isotope has been performed. No such γ-rays are, however, observed. Hence, in future experiments, which aim to investigate the ^{54}Ni isotope, the trigger conditions need to be optimised for the very long-lived predicted state. Furthermore, if such an analysis is to employ the same reaction as in the present analysis, a careful handling of the targets to minimize the contamination is necessary.

A largely extended level scheme of ^{53}Fe has been constructed as presented in PAPER V. The lifetimes of a few of the newly observed excited states have been measured and are presented in the thesis. The excitation energies and decay properties of these states are reproduced in large-scale shell-model calculations performed in the full fp shell. Also a limited investigation on effective g-factors has been performed. This study employs large-scale shell-model calculations, using the previously derived effective nucleon charges, and attempts to reproduce the experimentally determined branching ratios. However, no quantitative estimations on the effective g-factors can be derived from this investigation. A more extensive study using more experimental data is required.

Future work must extend the amount of experimental data for nuclei in the fp shell. Similar studies of electromagnetic properties as discussed in the present thesis should be employed to other mirror pair systems. This would provide additional information on the phenomenon of effective transition operators. In particular, an experiment dedicated to investigate the properties of the ^{54}Ni isotope has been proposed and accepted. This will take place within the RISING stopped beam campaign at Gesellschaft für Schwerionenforschung, GSI, in Germany, probably during the year 2005.

Chapter 6

Popularised Summary in Swedish

De atomer och molekyler som utgör materian i dagens universum, såsom vi känner det, är uppbyggda av många olika komponenter. Dessa komponenter har under årens lopp upptäckts genom diverse olika experiment. I början av 1900-talet upptäcktes att atomen har en inre struktur och består av en liten positivt laddad atomkärna omgiven av ett moln av elektroner. Senare experiment visade att atomkärnan i sig själv är uppbyggd av protoner och neutroner, gemensamt kallade nukleoner, vilka hålls sammans via den starka kärnkraften. Nukleonerna i sin tur uppvisar även de en inre struktur i form av kvarkar. Kvarkarna antas vara de fundamentala byggstenarna i materian omkring oss. De har sitt ursprung miljarder år tillbaka i tiden vid tidpunkten för universums skapelse.

Dagens forskning inom kärn- och partikelfysik strävar efter att försöka förstå och förklara de fundamentala egenskaper och förändringar som materian och dess olika byggstenar uppvisar under givna förhållanden. Exempelvis försöker vetenskapsmän återskapa det tillstånd som universums materia antas ha befunnit sig i strax efter Big Bang, vilket kräver extrema förhållanden vad gäller temperatur och densitet. I detta tillstånd antas kvarkarna, vilka normalt är bundna inne i nukleonerna, kunna röra sig fritt över en större volym. Under mer ”normala” förhållanden undersöks de parametrar som används för att beskriva atomkärnan. Utifrån dessa studier hoppas forskarna exempelvis på att få en djupare förståelse för de krafter som påverkar de individuella nukleonerna. De förhållanden som krävs för att genomföra studierna skapas vid stora anläggningar runt om i världen. Vid dessa anläggningar accelereras atomkärnor till höga hastigheter och tillåts kollidera med en annan atomkärna, vilket skapar det system av materia man önskar undersöka. De komponenter och signaler som bildas vid kollisionen registreras med avancerad detektorutrustning och därefter analyseras den insamlade datamängden.

I denna avhandling diskuteras olika aspekter av kärnreaktioner inducerade med tunga atomkärnor. En beskrivning av de experiment, detektorer och metoder som har använts återfinns tillsammans med en utförlig redogörelse av analysarbetet. De resultat som presenteras är baserade på dels experimentella data men även från simu-

leringar och teoretiska beräkningar.

Avhandlingen redogör för mätningarna av deuteroner och anti-deuteroner producerade vid acceleratorn RHIC (Relativistic Heavy-Ion Collider) på Brookhaven National Laboratory i USA. Vid tidpunkten för dessa mätningar accelererades guldkärnor upp till en hastighet väldigt nära ljusets innan de tilläts kollidera med varandra. Resultaten från dessa mätningar, vilka är de första för deuteroner och anti-deuteroner vid denna hastighet, presenteras och diskuteras.

Vidare i avhandlingen diskuteras mätningar av livstider av exciterade tillstånd i atomkärnor. Dessa mätningar baserar sig på data från experiment utförda vid LNL (Legnaro National Laboratory) i Italien där atomkärnor accelererades upp till ett par procent av ljusets hastighet innan kärnreaktionerna ägde rum. De uppmätta livstiderna kan användas för att undersöka fundamentala elektromagnetiska egenskaper hos kärnorna. Speciellt redogörs för hur livstidsmätningar i så kallade spegelkärnor, vilka är par av kärnor där antalet protoner och neutroner är det omvända, kan användas för att bestämma effektiva nukleonladdningar. Dessa introduceras i gängse teoretiska modeller för att ge en bättre överensstämmelse mellan teori och experiment. Speciellt fokuserar avhandlingen på livstidsresultat för spegelkärnorna $^{51}_{26}\mathrm{Fe}_{25}$ och $^{51}_{25}\mathrm{Mn}_{26}$. Metodiken och de erhållna resultaten från denna studie diskuteras utförligt.

Acknowledgements

I would like to express my gratitude to everyone who has, in one way or another, been involved in the present thesis. All colleagues and friends at the Division of Nuclear Physics and the former Division of Cosmic and Subatomic Physics are acknowledged for their help and support over the years. In particular, I would like to thank the persons I have been working closest with:

Claes Fahlander, for giving me the contingency to continue and complete my thesis work within his research group. I thank him for his encouragement and motivation in this work as well as the introduced poker sessions, which enriched my life in several differnt aspects.

My supervisor, Dirk Rudolph, mainly for his excellent guidance, valuable advice, and expertise in nuclear physics, but also for introducing me to "Doppelkopf".

Hans-Åke Gustafsson, together with Anders Oskarsson and Evert Stenlund, for their knowledge, encouragement, and guidance during the time I spent working within the group for Relativistic Heavy-Ion Physics.

Joakim Nystrand, for encouraging and introducing me to search for deuterons and anti-deuterons. His help and guidance in the analysis work is greatly appreciated.

My fellow students and moreover roommates over the years, Henrik Tydesjö and Jörgen Ekman, for their assistance and support on various issues as well for sharing great fun, not only within the walls of the physics deparment, and for beeing good friends.

Lennart Österman for countless small favours, discussions and help with computers whenever needed.

I also wish to thank the rest of the Nuclear Structure Group; Lise-Lotte Andersson, Joakim Cederkäll, Andreas Ekström, Emma Johansson, Margareta Hellström, Milena Mineva, and Hans Ryde for valuable discussions and for creating a nice and friendly atmophere to work in. The former students Pavel Golubev, Paul Nilsson, and David Silvermyr are acknowledged for their help on various issues. Furthermore, I also would like to thank my friends for their support and for all good moments shared over the years.

I gratefully acknowledge the financial support from Lund University, the Swedish House of Nobility, NORDITA (Nordic Institute for Theoretical Physics), Legnaro National Laboratory, and Kungliga Fysiografiska Sällskapet i Lund.

Finally, I would like to express my sincere gratidude to my family for their encouragement and support throughout the years.

Appendix A

Parameterization of the cross sections

Due to the limited amount on experimental data on total cross sections for deuteron and anti-deuteron induced interactions, a direct parameterization of the cross section on a nucleus A is not possible. Instead, a method has been developed, which calculates the inelastic deuteron (anti-deuteron) cross section from the inelastic cross sections for protons (anti-protons), $\sigma_{p,A}$ ($\sigma_{\bar{p},A}$), and neutrons (anti-neutrons), $\sigma_{n,A}$ ($\sigma_{\bar{n},A}$). The parameterization for $\sigma_{p,A}$, $\sigma_{\bar{p},A}$, $\sigma_{n,A}$, and $\sigma_{\bar{n},A}$ is taken from Ref. [44], where the inelastic (anti-)helium cross section is calculated using

$$\begin{aligned}
\sigma_{p,A}(E) = \;& 45 \cdot A^{0.7} \cdot [1 + 0.016 \sin(5.3 - 2.63 \ln A)] \cdot \\
& \cdot [1 - 0.62 \exp(-5E) \sin(1.58 \cdot E^{-0.28})], \\
\sigma_{\bar{p},A}(E) = \;& A^{2/3} \cdot [48.2 + 19 \cdot (E - 0.02)^{-0.55} - 0.106 \cdot A^{0.927} \cdot E^{-1.2} + \\
& + 0.059 A^{0.927} + 0.00042 A^{1.854} \cdot E^{-1.5}], \\
\sigma_{n,A} = \;& (43.2 \pm 2.3) \cdot A^{0.719 \pm 0.012}, \\
\sigma_{\bar{n},A} = \;& A^{2/3} \cdot (51 + 16 \cdot E^{-0.4}).
\end{aligned} \tag{A.1}$$

The cross sections are given in mb and the parameter E is the kinetic energy of the nucleon in GeV. The effective nucleon-nucleus cross section, $\sigma_{N,A}$,is calculated as the average of the neutron- and proton-nucleus cross section,

$$\sigma_{N,A} = \frac{\sigma_{p,A} + \sigma_{n,A}}{2}, \tag{A.2}$$

and similarly for anti-nucleons.

The parameterization of the inelastic deuteron cross section, $\sigma_{d,A}$, on nuclei is derived as follows. The cross section on a nucleus A can be written as

$$\sigma_{d,A} = \sigma_{N,A} + \Delta\sigma_{d,A}, \tag{A.3}$$

where $\Delta\sigma_{d,A}$ is the difference in cross section compared to the nucleon-nucleus cross section. A geometric picture of the nuclear collisions is illustrated in Fig. A.1. Based

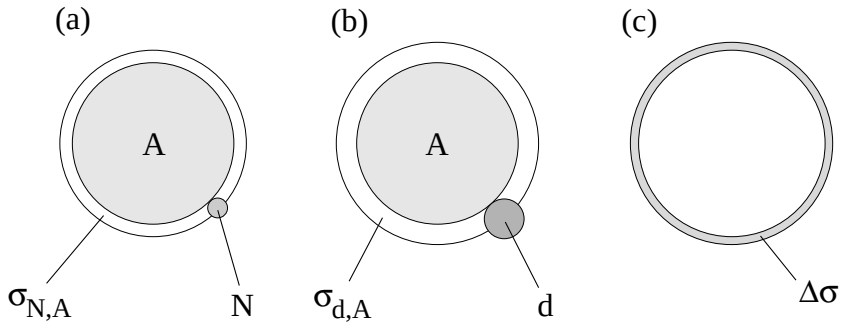

Figure A.1: *Geometric picture used for the parameterization of the (anti-)deuteron cross section. Panels (a) and (b) illustrate the nucleon-nucleus, $\sigma_{N,A}$, and the deuteron-nucleus, $\sigma_{d,A}$, cross section, respectively. The cross section difference, $\Delta\sigma$, is illustrated in panel (c).*

on this geometry the deuteron cross section can be written as

$$\sigma_{d,A} = [\sqrt{\sigma_{N,A}} + \Delta_d(A)]^2, \tag{A.4}$$

from which $\Delta_d(A)$ can be expressed as

$$\Delta_d(A) = \sqrt{\sigma_{d,A}} - \sqrt{\sigma_{N,A}}. \tag{A.5}$$

$\Delta_d(A)$ corresponds to the average difference in radius between a nucleon and a deuteron, which can be expected to be largely independent of the nuclear mass number and the collision energy. Comparison with experimental deuteron data [45, 46] gives that $\Delta_d(A) = 3.51(25)$ mb$^{1/2}$ independent of A.

In Ref. [44] it is assumed that the anti-helium cross section can be written in the same way as the helium cross section. Following this approach, the inelastic anti-deuteron cross section, $\sigma_{\bar{d},A}$, can be written as

$$\sigma_{\bar{d},A} = [\sqrt{\sigma_{\bar{N},A}} + \Delta_{\bar{d}}(A)]^2, \tag{A.6}$$

where

$$\sigma_{\bar{N},A} = \frac{\sigma_{\bar{p},A} + \sigma_{\bar{n},A}}{2}. \tag{A.7}$$

The difference in radius between an anti-nucleon and an anti-deuteron, $\Delta_{\bar{d}}(A)$, is assumed identical to the difference between a nucleon and a deuteron. Hence, the constant value $\Delta_{\bar{d}}(A) = 3.51(25)$ mb$^{1/2}$ is used.

Bibliography

[1] K.S. Krane, "Introductory Nuclear Physics", John Wiley & Sons, New York (1988).

[2] K.L.G. Heyde, "The Nuclear Shell Model", Springer Verlag, Heidelberg (1994).

[3] J. Ekman, Ph.D. thesis, Lund University (2004), ISBN 91-628-6061-5.

[4] J.D. Bjorken, Phys. Rev. D **27** (1983) 140.

[5] J.W. Harris and B. Müller, Ann. Rev. Nucl. Part. Sci. **46** (1996) 71.

[6] U. Heinz and B.V. Jacak, Ann. Rev. Nucl. Part. Sci. **49** (1999) 529.

[7] GAMMASPHERE, The Beginning ... 1993-1997, Science Highlights booklet, Ed. M.A. Riley, (1998); http://nucalf.physics.fsu.edu/∼riley/gamma

[8] G.D. Westfall *et al.*, Phys. Rev. Lett. **37** (1976) 1202.

[9] C. Rossi Alvarez, Nuclear Physics News, Vol. 3, 3 (1993).

[10] A. Dewald *et al.*, Nucl. Phys. **A545**, 822 (1992).

[11] A. Dewald *et.al.*, Z. Phys. A **334** (1989) 163-175.

[12] G. Böhm *et al.*, Nucl. Inst. Meth. A **329** (1993) 248-261.

[13] http://www.ikp.uni-koeln.de

[14] I.Y. Lee, Nucl. Phys. A **520** 641c (1990).

[15] D.G. Sarantites *et al.*, Nucl. Inst. Meth. A **383** 506 (1996).

[16] D.G. Sarantites *et al.*, to be published.

[17] C. Andreiou, Ph.D. thesis, Lund University (2002), ISBN 91-628-5308-2.

[18] http://www.phenix.bnl.gov

[19] D.P. Morrison *et al.*, (PHENIX Collaboration), Nucl. Phys. A **638** (1998) 565.

[20] F. Sauli, CERN preprint 77-09 (1977).

[21] S.T. Butler and C.A. Pearson, Phys. Rev. **129** (1963) 836.

[22] A.Z. Mekjian, Phys. Rev. C **17** (1978) 1051.

[23] L.P. Csernai and J.I. Kapusta, Phys. Rep. **131** (1986) 223.

[24] W.R Leo, "Techniques for Nuclear and Particle Physics Experiments", Springer-Verlag, New York, (1994).

[25] T. Chujo *et al.*, (PHENIX Collaboration), Nucl. Phys. **A715** (2003).

[26] A. Polleri, J.P. Bondorf and I.N. Mishustin, Phys. Lett. B **419** (1998) 19.

[27] H. Morinaga and T. Yamazaki, "In-Beam Gamma-Ray Spectroscopy" North-Holland Publishing Company, Amsterdam, New York, Oxford, 1976.

[28] K. Heyde, "Basic Ideas and Concepts in Nuclear Physics", Institute of Physics Publishing, Bristol (1994).

[29] A. Bohr and B.R. Mottelson, "Nuclear Structure Vol. 2",Benjamin Inc., New York, 1975.

[30] E. Caurier, shell model code ANTOINE, IRES, Strasbourg 1989-2002.

[31] E. Caurier, F. Nowacki, Acta Phys. Pol. **30**, 705 (1999).

[32] M.A. Bentley *et al.*, Phys. Rev. C **62**, 051303(R) (2000).

[33] J. Ekman *et al.*, Eur. Phys. J. A **9**, 13 (2000).

[34] J. Ekman *et al.*, Phys. Rev. C **70**, 014306 (2004).

[35] A. Poves, J. Sanchez-Solano, E. Caurier, and F. Nowacki, Nucl. Phys. **A694**, 157 (2001).

[36] W.A. Richter *et al.*, Nucl. Phys. A **523**, 325 (1991).

[37] S.J. Williams, Ph.D. thesis, Keele University (2003).

[38] J. Huo, H. Sun, W. Zhao and Q. Zhou, Nucl. Data Sheets **68** 887 (1993).

[39] D. Rudoplh *et al.*, Eur. Phys. J. A **4**, 115 (1999).

[40] A. Gadia *et al.*, private communications.

[41] J. Ekman, "Isospin Symmetry Breaking in the A=51 Mirror Nuclei", Licentiate thesis, Department of Physics, Lund University (2002).

[42] M. Weiszflog *et al.*, Eur. Phys. J. A **11**, 25 (2001).

[43] S.J. Williams, Phys. Rev. C **68**, 011301 (2003).

[44] A.A.Moiseev and J.F.Ormes in Astroparticle Physics 6(1997) 379-386.

[45] J.Jaros et al., Phys. Rev. C18(1978)2273.

[46] E.O.Abdurakhmanov et al., Z. Phys. C5(1980)1.